

Signatures of Midsummer Droughts Over Central America and Mexico

Zijie Zhao (✉ zijizhao@student.unimelb.edu.au)

The University of Melbourne School of Earth Science <https://orcid.org/0000-0003-3403-878X>

Meng Han

University of Tasmania Institute for Marine and Antarctic Studies

Kai Yang

University of Tasmania Institute for Marine and Antarctic Studies

Neil J Holbrook

University of Tasmania Institute for Marine and Antarctic Studies

Research Article

Keywords: Midsummer Drought, Central America, Mexico, Madden–Julian Oscillation, El Niño–Southern Oscillation, Statistical Modelling

Posted Date: April 20th, 2022

DOI: <https://doi.org/10.21203/rs.3.rs-1512893/v1>

License: © ⓘ This work is licensed under a Creative Commons Attribution 4.0 International License.

[Read Full License](#)

Abstract

The annual cycle of precipitation over Central America and Mexico is climatologically characterized by a robust bimodal distribution, normally termed as the midsummer drought (MSD), influencing a large range of agricultural economic and public insurances. Compared to the studies focusing on the mechanisms underpinning the MSD, less research has been undertaken related to its climatological signatures. This is due to a lack of generally accepted methods through which to detect and quantify bimodal precipitation accurately. The present study focuses on characterizing the MSD climatological signatures over Mexico and Central Mexico between 1979 and 2017. This was completed using a new method of detection. The signatures were analyzed from three aspects, namely 1) climatological mean states and variability; 2) connections with large scale modes of climate variability (El Niño–Southern Oscillation (ENSO) and the North Atlantic Subtropical High (NASH)); and 3) the potential afforded by statistical modelling. The development of MSDs across the region is attributed to changes of surface wind – pressure composites, characterized by anomalously negative (positive) surface pressure and onshore (offshore) winds during the peak (trough) of precipitation. ENSO's modulation of MSDs is also shown by modifying the surface wind – pressure patterns through MSD periods, inducing the intensified NASH and associated easterlies from the Caribbean region, which induce relatively weak precipitation at corresponding time points and subsequently intensify the MSD magnitude and extend the MSD period. Building on previous research which showed MSDs tend to start/end in Madden-Julian Oscillation (MJO) phases 1 and 8, a fourth–order polynomial was used here to statistically model the precipitation time series during the rainy season. We show that the strength of the bimodal precipitation can be well modelled by the coefficient of the polynomial terms, and the intra-seasonal variability is largely covered by the MJO indices. Using two complete MJO cycles and the polynomial, the bimodal precipitation during the rainy season over Central America and Mexico is synoptically explained, largely contributing to our understanding of the MJO's modulation on the MSD.

1 Introduction

The atmospheric circulation of Central America and Mexico plays an important role in the global climate. This includes the close connection between the region and large–scale modes of climate variability, such as El Niño–Southern Oscillation (ENSO) and the North Atlantic Subtropical High (NASH) (Díaz et al., 1994, Mapes et al., 2005, Curtis and Gamble, 2008, Gamble et al., 2008, Peralta-Hernández et al., 2008). The region is characterized by steep topography and is bounded to the west by the North Pacific Ocean and to the east by the North Atlantic Ocean (specifically the Gulf of Mexico and the Caribbean Sea). The strong easterly trade winds are modified by this topography across Central America and Mexico, dividing the whole area into two major climate regions identified here as the Pacific side and the Caribbean side.

On the Pacific side of the domain, the annual precipitation cycle is largely dominated by a bimodal distribution (Magaña et al., 1999, Taylor and Alfaro, 2005, Amador et al., 2006), characterized by the first precipitation peak between May and June, a reduction in precipitation typically between July and August, and a second precipitation peak between late August and early October. During the first precipitation

peak, the warming of the eastern Pacific enhances convection and is accompanied by a weakening of the easterlies. Then, the decrease in precipitation, known as the “mid-summer drought” (Magaña et al., 1999), follows with the cooling of the ocean around the Pacific coast from July to August. The second precipitation peak is characterized by relatively weak trade winds and a warmer eastern Pacific. The mid-summer drought (MSD) can represent a precipitation reduction by up to 40% (Small et al., 2007), a change that amounts to a dominant proportion of the annual precipitation variability (Curtis, 2002).

The annual rainfall over the Caribbean side is more complex in terms of the spatial variability. While some studies report that MSDs are generally absent along the Caribbean coast of Central America (Magaña et al., 1999, Taylor and Alfaro, 2005, Small et al., 2007, Amador, 2008), it has been observed that similar bimodal precipitation cycles exist over the Greater Antilles (Chen and Taylor, 2002, Taylor et al., 2002, Spence et al., 2004, Ashby et al., 2005) and parts of the Caribbean side of Central America (Maldonado et al., 2016). Similar to MSDs on the Pacific side of Central America and Mexico, the rainfall reduction over the Caribbean side demonstrates a tight connection with the Caribbean Low–Level Jet (CLLJ), a moisture transport mechanism carrying reduced moisture flux from the Caribbean Sea that subsequently suppresses the convection system (Magaña et al., 1999, Wang, 2007, Muñoz et al., 2008, Amador, 2008, Whyte et al., 2008).

Since the MSD was first identified in the 1960s (Portig, 1961), various theories have been proposed to explain its origins and the development of its bimodal signature. Magaña et al. (1999) suggested that the MSD–sea surface temperature (SST)–radiation relationship, which uses the enhancement/suppression of convection induced by the warming/cooling of SST, explains the bimodal precipitation over the Pacific coast of Central America and Mexico. This theory was later revised recognizing the important role of the trade winds, and importantly the CLLJ, in the development of the MSD (Magaña and Caetano, 2005, Herrera et al., 2015). The NASH and its westward intensification have been recognized as an important contributor to the development of the MSD in various studies, which induces an associated strengthening of the CLLJ moisture transport (Mestas-Núñez et al., 2007, Small et al., 2007, Wang et al., 2007, 2008). Other factors, including mountain - gap winds over Central America (Romero-Centeno et al., 2003, 2007), the seasonality of tropical cyclones (Curtis, 2002, Inoue et al., 2002, Small et al., 2007, Liebmann et al., 2008), vertical wind shear and atmospheric particles (Angeles et al., 2010), solar declination (Karnauskas et al., 2013), and the Madden–Julian Oscillation (MJO: Perdigón-Morales et al., 2019, Zhao et al., 2019), have also been shown to play a role in the generation or modulation of MSDs and their associated large- or local-scale climate patterns.

Although numerous studies have focused on the physical mechanisms that cause MSDs and the signatures and annual characteristics of the bimodal precipitation, including its detection and quantification of its climatology and variability, these studies have lacked fine-scale detail of the temporal and spatial variability. Mosiño and García (1966) determined MSDs by finding consecutive months characterized by decreased precipitation relative to those exhibiting precipitation maxima that bounded them during the rainy season (May to October). After slight modification, this method was later applied to examine MSDs over Mexico using Climate Hazards Group InfraRed Precipitation with Station data and

subsequently quantified their duration and intensity using a self-defined monthly index (Perdigón-Morales et al., 2018). Using second-order harmonic regression, Curtis (2002) demonstrated that the bimodal signature of the MSD accounted for most annual precipitation variability over Central America, and this tendency can be strengthened during positive ENSO phases. Karnauskas et al. (2013) provided the first global distribution of bimodal precipitation using several observations, demonstrating that the MSD is a climate signal that is detectable at the global scale, albeit that it is significant in specific regions, including Central America and Mexico. Maldonado et al. (2016) argued that MSDs can exist over both the Caribbean and Pacific sides of Central America, and the intensity and magnitude of those MSDs on the Pacific side are more significantly connected with the CLLJ and ENSO. Most previous studies that have examined the signature of MSDs were conducted using monthly precipitation data from an average annual cycle, limiting the potential of the results to reveal the interannual variability of MSDs at fine resolution.

Here, we investigate the MSD across Central America and Mexico using daily precipitation observations, with a focus on identifying the: 1) mean states and variability, 2) connection with large-scale modes of climate variability (specifically, ENSO and the MJO), and 3) potential to skillfully statistically model the MSD.

2 Data And Methods

2.1 Data

This study uses the Climate Prediction Center (CPC) global unified gauge-based analysis of daily precipitation (Xie et al., 2007, Chen et al., 2008) from 1979 – 2017 to quantify the bimodal signature of precipitation annually and interannually across Central America and Mexico, the domain is shown in Figure 1. The CPC data were constructed on a $0.5^{\circ}0.5^{\circ}$ spatial grid using observed data from various sources. In this dataset, the daily climatology was calculated by summing the first six harmonics of the annual climatological (average) cycle, with the adjustment from the Parameter-Elevation Regressions on Independent Slopes Model (PRISM) monthly climatology (Daly et al., 1994, 2002), which is a climate analysis system providing criteria for the evaluation of climate properties. The daily precipitation ratio with respect to the climatology was obtained by optimal interpolation methods. The CPC data have been widely used in previous studies associated with precipitation (e.g., Preethi et al., 2011, Hou et al., 2014) and their quality have been evaluated against both observations and model simulations using various statistical methods (e.g., Katiraie-Boroujerdy et al., 2013, Rana, et al., 2015).

In this study, properties used to characterize climate states across the region, including 2m (above the surface) temperature, 10m horizontal winds, and surface pressure, were extracted from the ERA-Interim reanalysis data (Dee et al., 2011) for the domain (120°W - 60°W , 0° - 30°N) on a $0.5^{\circ}0.5^{\circ}$ spatial grid, from 1979 – 2017. The gridded three-hourly data were averaged into daily values. Sea surface temperature (SST) data from 1982 – 2017 were obtained from the NOAA OI SST V2 dataset (Reynolds et al., 2007, Huang et al., 2021) over the same domain on a $0.25^{\circ}0.25^{\circ}$ grid, while for the period from 1979 – 1981 the

data were obtained by re-gridding ERA–Interim reanalysis data onto a $0.25^{\circ}0.25^{\circ}$ grid since NOAA data do not cover this period.

The ENSO index used in this study is the Oceanic Niño Index (ONI) based on ERSSTv5 data (Huang et al., 2017), which is calculated as 3-month running mean SST anomalies in the Niño3.4 region (5°N - 5°S , 120° - 170°W). Warm and cold periods over the record are identified when the $\pm 0.5^{\circ}\text{C}$ threshold is met for five consecutive overlapping three-month periods, or longer. Subsequently, El Niño/La Niña years are determined by finding the years when ONI values, in at least five months during September to next year's February, meet the threshold. The original ONI from September to February is averaged in each year to get the annual ONI, which is used to quantify the interannually-varying phase and magnitude of ENSO.

The MJO index used in this study was developed using a seasonally independent index based on paired empirical orthogonal functions of the combined fields of near-equatorially averaged 200 hPa and 850 hPa zonal winds, and satellite-observations of outgoing longwave radiation (OLR) data, the resultant principal component (PC) time series are termed the Real–time Multivariate MJO series 1 and 2 (RMM1 and RMM2: Wheeler and Hendon, 2004). This index has been shown to effectively capture the interannual modulation of the global variance induced by the MJO, as well as having the potential to reconstruct a variety of weather patterns induced by the variance in MJO activity. Based on the RMM index, daily MJO responses are classified into eight phases, which demonstrate an approximately anticyclonic propagation from phase 1 to phase 8.

2.2 MSD detecting algorithms

The detection of annual MSD events is achieved using the method recently proposed by Zhao et al. (2020). In this method, the MSD signal in a precipitation time series is detected from the first peak maximum (onset of MSD) of the bimodal precipitation to the second peak maximum (end of MSD), covering the whole period of the precipitation reduction. This detection was achieved by two consecutive steps. First, the seasonally varying climatology of precipitation was smoothed using a 31–day Gaussian filter at each grid point, and the climatological MSD signal at each grid point was determined following three criteria: 1) two local precipitation peaks, P1 and P2, should exist separately within the periods from May 15th to July 15th and August 15th to October 15th, respectively, and their corresponding dates recorded as onset and end dates, 2) the annual maximum precipitation value should be on either the onset or end date, and 3) the linear trend fitted from the first day of the year to the onset date should be positive and statistically significant at the 95% confidence level, and the trend fitted from the MSD-end date to the last day of the year should be negative and also statistically significant at the 95% level, the locations where these precipitation criteria are met are termed the MSD areas. Second, the same criteria were applied to annual precipitation smoothed using a 31–day Gaussian filter at each grid point across the MSD area to show the distribution of the annual MSD signals. Compared to previous methods, most of which detect and quantify the MSD at the monthly climatological scale, this algorithm ensures that the MSD signals are resolved at the daily scale, enabling a more practical detection for studies focusing on MSD signatures. The code is publicly available via <https://github.com/ZijieZhaoMMHW>.

During the detection, some metrics are determined to describe or quantify the corresponding MSD signal, including onset, end and peak (corresponding to the minimum precipitation during MSD signals) dates, duration (period from onset to end date) and intensity of MSD (I_{msd} , García-Martínez, 2015) calculated following $I_{msd} = \frac{P_{max} - P_{min}}{P_{max}}$, where P_{max} is the larger one in precipitation on onset and end dates and P_{min} is the average precipitation through the MSD signal. In this study, the detection of annual MSD signals was executed for CPC precipitation data over the period from 1979 to 2017 in the domain (120°W-60°W, 0°-30°).

2.3 Anomalies and composites

The anomaly for a particular time series was calculated by removing the climatological annual cycle in Julian days, where data on February 29th in each non-leap year was filled by the mean of that on February 28th and March 1st. This step may also be achieved by removing the first several harmonics (e.g., Oliver and Holbrook, 2018), but we calculated this here based on the elimination of means in each corresponding Julian day to get a more robust signature of the long-term climatology. Here, anomalies were calculated for CPC precipitation, 2m temperature, 10m horizontal winds, surface pressure and SST.

The climate composite (normally termed as the 'composite' in this study), used to characterize the mean states of a climate property through a particular time-period, is calculated by temporally averaging the climate property across the corresponding time points. The advantage of this approach is to ensure the continuity of the calculated composite at both the spatial and temporal scales, which could generate more physically explainable patterns. Similar approaches have been used by Oliver et al. (2018).

3 Results

3.1 Mean states

The climatological signatures of detected MSDs over Central America and Mexico, including frequency (Figure 2a), mean onset (Figure 2b), peak (Figure 2c) and end (Figure 2d) dates, and calculated climatological MSD intensity (I_{msd}) (Figure 2f), show significant spatial variabilities. The generally high frequencies of the detected MSD signals reveal robust bimodal characteristics of annual precipitation over most parts of the domain, including the Pacific coast of southern Mexico and Central America, Yucatán Peninsula, coasts around the Gulf of Mexico and Cuba. To the southeast, detected MSD signals tend to start earlier and end later, corresponding to relatively longer climatological durations (Figure 2e). Compared to other signatures, the mean peak dates of the MSD signals show higher spatial variabilities, indicated by more noisy signals and irregular spatial patterns. Several areas exhibiting climatologically intense and long MSDs can be identified, including the Pacific coast of Central America, and coastal areas around the Gulf of Mexico and Cuba.

The temporal variability of MSD signals is also examined. The proportion of areas exhibiting MSD events demonstrates a time series with high frequency at the interannual scale (Figure 3a). The time series does not have significant autocorrelation (Figure 3b), implying its predictability cannot be modelled by an autoregressive model, and which has been widely used in studies associated with predictions of climate indexes (e.g., Seo et al., 2009, Ubilava and Helmers, 2013, Oliver and Thompson., 2016). The time series is also shown to have no correlations with other large-scale climate modes, such as ENSO and the Pacific decadal oscillation (PDO) (not shown here), which is consistent with previous research (Fallas-López and Alfaro, 2012). Additionally, there is no significant linear trend in the time series. Generally, the annual number of MSD signals over the domain can thus be interpreted as a complex time series with significant interannual variability, which may not be well modelled by its own autocorrelation characteristics.

By spatially averaging the major characteristics of MSD signals (onset, peak and end dates, duration, and I_{msd}) in each year, the temporal variabilities of MSD signatures are explored. The cross-correlation among the five signatures and annual ONI show a well-organized pattern (Figure 4). The onset/end date has significantly negative/positive correlation with the duration, which is intuitively reasonable. The I_{msd} is positively correlated with the duration, indicating that a stronger intensity MSD signal is also generally part of a longer duration event. It is specifically notable that the annual ONI is positively correlated with both the duration and I_{msd} , indicating that stronger and longer MSD signals tend to exist in El Niño years instead of La Niña years.

Large-scale climate composites of key characteristics of MSD signals are also examined. The climate composites of six properties (anomalies of precipitation, 2m temperature, 10m horizontal winds, surface pressure and sea surface temperature) over the domain were calculated for three time points (onset, peak and end dates of the MSD signals) to illustrate the changes of climate patterns during the generation of the MSD (Figure 5). The anomalously positive precipitation over the domain exists during the onset and end dates of MSD signals, while opposite patterns are determined for peak dates, corresponding to the bimodal characteristics of MSD signals. Significant wind shifting during the development of MSD signals is notable. When the MSD starts over Central America and Mexico, the Pacific coast of Central America and coastal areas around the Gulf of Mexico – where robust MSD signals are found – are dominated by onshore wind anomalies. These enhanced onshore winds together contribute to a low-pressure (cyclonic) system, correspondingly inducing anomalously negative near surface temperature anomalies over both land and ocean. Then, these onshore wind anomalies transition into enhanced offshore wind anomalies on the peak dates of the MSD signals, accompanied by a corresponding high pressure (anticyclonic) system and anomalously positive near surface temperature. The climate composites on the end dates of the MSD signals are remarkably similar to those on the onset dates, indicating the retrieval process from peak to end of MSDs. The precipitation reduction on the peak date of the MSD is accompanied by strong trade wind easterlies, which may be largely due to the enhancement of the CLLJ during July to August, transporting moisture (flux) from the Caribbean region and subsequently suppressing the convection. The influence of the NASH is not significant in the climatological composites.

3.2 Connections with ENSO and the MJO

According to previous studies (Magaña et al., 1999, 2003, Chen and Taylor, 2002, Curtis, 2002, Peralta-Hernández et al., 2008, Hidalgo et al., 2017), MSDs are highly variable interannually. MSDs can be modulated by ENSO and/or the MJO, as has been shown previously for the generation and development of the MSD in Costa Rica (Martin and Schumacher, 2011, Perdigón-Morales and Romero-Centeno, 2019, Zhao et al., 2019, 2020). In this section, we further explore the connection between MSDs and both ENSO (Section 3.1) and the MJO (Section 3.2) across Central America and Mexico over the period from 1979 – 2017.

3.2.1 ENSO

The climatological precipitation over Central America and Mexico in each ENSO phase is separately calculated for June, July, August and September. Choosing the three time-segments is undertaken to better illustrate the variabilities of precipitation during common MSD periods (e.g., Rauscher et al., 2008, Corrales-Suastegui et al., 2020). In El Niño years, generally negative precipitation anomalies exist in most parts of the region, including the Pacific Coast of the domain and coastal areas around the Gulf of Mexico, where MSD signals with high frequency are detected from June to September (Figure 6a-c). It is notable that areas exhibiting bimodal precipitations, such as the Pacific side of Central America, tend to be dominated by suppressed precipitation during July and August in positive ENSO phases. Opposite patterns exist in La Niña years (Figure 6d-f), indicating relatively wet rainy seasons in the July-August period over most parts of the domain.

The climate composites of surface pressure and 10m winds in each ENSO phase at onset, peak and end dates are shown in Figure 7. Compared to climatological composites shown in Figure 5, some biases exist in these patterns. For ENSO-neutral years, the composites of near-surface winds and pressures are broadly similar to the climatological states (cf. Figure 5g, h, i), except with relatively weak cyclonic/anticyclonic patterns and more significant influences of the NASH. For El Niño years, the anomalous cyclonic system during the onset of the MSD in the Caribbean Sea region, on the peak MSD dates, the climatological onshore wind anomalies at the Pacific coast of Central America (Figure 5i) are replaced by anomalous easterly winds from the Caribbean Sea, which is due to the westward extension of the NASH. The influence of the NASH in El Niño years is more significant, shown by the westward extension of the high-pressure centre through the entire MSD period. For La Niña years, the wind-pressure patterns at the MSD onset and end dates are similar to the climatological patterns, while anomalous westerly winds pass through Central America on the peak dates, making the climatological anticyclonic system (Figure 5h) absent. For precipitation anomalies in El Niño years, the generally drier June and September reveal that the precipitation during the two months is lower than climatology. The two months may still be in potential MSD periods, and the onset/end dates of corresponding MSD events may thus be extended to some days in May/October. These features indicate relatively long MSD periods (shown by longer durations of MSD signals) during El Niño years, which is consistent with the positive correlation between MSD durations and ONI shown in Figure 4. The anomalously high precipitation on the peak dates of the MSD in La Niña years indicates a relatively “shallow” trough of precipitation reduction, corresponding to relatively weak MSD signals (shown by smaller I_{msd} of MSD signals).

Generally, ENSO's modulation of the MSD over Central America is achieved by modifying the low-level wind-pressure system. In positive ENSO phases (El Niño years), the NASH strengthens during the MSD, especially from the peak to end dates. On the peak date of the MSD, the westward extension of the NASH brings stronger easterlies, inducing a more intense CLLJ. The intensified CLLJ can last to late boreal summer and remain through to the end date of the MSD, inducing a drier MSD throughout, since the moisture flux associated with the easterly flow suppresses the convection. This feature makes MSDs in El Niño years more intense (larger I_{msd}) and longer, resulting in a generally drier summer. In negative ENSO phases (La Niña years), the influence of the NASH tends to be insignificant and the peak of the CLLJ is suppressed. The easterlies on the peak date of the MSD is replaced by strong westerlies from the Pacific, inducing a wetter MSD period and a "shallower" MSD trough.

Another factor to induce the synchronicity between the change of wind-pressure patterns modulated by ENSO and precipitation during the MSD may be the interaction between the winds and topography – that is, the onshore/offshore winds and orographic forcing associated with steep mountainous terrains. Due to the orographic uplifting, the interaction between the onshore winds and orography act to enhance the precipitation, while offshore winds tend to have the opposite effect. The shifting of wind patterns over the major MSD areas (the Pacific Coast of Central America and coasts around the Gulf of Mexico) can contribute to the bimodal shape of MSD signals. Therefore, it can be deduced that changes of wind patterns in ENSO years may influence the interannual variability of MSD signals. Similar features have been observed in Central America (e.g., Zhao et al., 2020).

3.2.2 MJO

To analyze the connection between the MSD signals across the domain and the MJO (RMM1 and RMM2), each detected MSD signal is categorized into four periods. To represent the typical signatures of the MSD signals in the different MJO phases, each period is separated based on a particular percentile. For each MSD signal, P1 is from the onset date to the 30th percentile between the onset date and the peak date, while P2 follows P1 and ends in the peak date. Similarly, P3 follows P2 and ends in the 70th percentile between peak dates and end dates, while P4 covers the remained period. This is illustrated in Figure 8. Each period of the MSD has a physical meaning. P1 and P4 represent relatively short periods during the onset and end of MSD signals, so they could be intuitively named as the "onset period" and "end period". We refer to P2 as the "development period", which spans between the onset and peak date, that is the period when precipitation tends to reduce. We refer to P3 as the "recovery (or decay) period", when the summer precipitation recovers towards its second peak.

Based on this definition, the temporal connection between MSD periods and MJO phases were analyzed by directly calculating the percentage fraction of each MSD period that occurs during each MJO phase (Figure 9) – i.e., totals at each individual grid point across all MJO phases should sum to unity (1). While P2 and P3 do not exhibit clear signatures of specific correspondences to MJO phase, P1 and P4 however show strong correspondences with MJO phase 8-1 in areas exhibiting robust bimodal precipitation signatures, such as the Pacific coast of southern Mexico and Central America and Cuba. This is also

notable in phases 2-3 but not quite as strong. This signature indicates that detected MSD signals tend to onset/end in MJO phase 8–1 over the domain.

The MJO phases also modulate the near surface wind–pressure patterns. Figure 10 shows the wind–pressure composites corresponding to MJO phases during the period when MSD signals are detected. In MJO phases 8–1, westerly anomalies with approximate geostrophic balance approach the Pacific Coast of Central America, which subsequently reach the Caribbean region and become southwesterly to form a low–pressure system centered in the Gulf of Mexico. The westerlies from the Pacific weaken in MJO phases 2–3, shown by their general geostrophic balance and weaker meridional pressure gradient. This result indicates the strength of the westerlies from the Pacific associated with the MJO phases is positively correlated with the onset/end of the MSD events along the Pacific coast of Central America and Mexico. Specifically, the westerlies and their associated convergence zone can induce strong convection and enhanced precipitation, corresponding to the precipitation maxima at the dates of MSD onset and end. This is consistent with previous MSD-MJO related-research for Costa Rica (Zhao et al., 2019), but here extending over the larger domain that includes most parts of the Pacific coast of Central America and southern Mexico. In MJO phases 4–5 and 6–7, easterly anomalies from the Caribbean Sea contribute to a divergence system centered over the Gulf of Mexico, which suppresses the precipitation and subsequently induces the dry trough of the MSD signal.

3.3 Statistical modelling of the MSD.

In this section, we examine the statistical modelling potential of the bimodal precipitation signature over Central America and Mexico and infer possible physical mechanisms underpinning this. In MSD areas, the rainy season is characterized by two peaks and a trough in the summertime precipitation time series. Although only the trough of precipitation is referred to as the MSD signal in our definition, the increase/decrease of precipitation before/after the MSD (trough) also plays an important role in characterizing the variability of annual precipitation time series since it is very different from other dry seasons. Further, we statistically model not only the MSD signals (from onset to end), but also the whole precipitation time series in the rainy season, which accounts for most of the annual variabilities.

We first confirm the definition of what is meant by the rainy season. Over Central America and Mexico, the rainy season is typically termed the period from May to October in associated research about the MSD (Hastenrath, 1967, Magaña et al., 1999). However, this definition is based on the climatological unimodal precipitation maximum in most areas of the northern hemisphere, which may not be adaptable to bimodal precipitation climatologies that characterize MSD regions. Therefore, we specifically define here the rainy season for MSD areas in this study.

After calculating the seasonally varying climatology of precipitation at each grid point across the region characterized by MSD occurrences, and smoothing it using a Gaussian filter, an empirical orthogonal function (EOF: Lorenz, 1956) analysis is applied to the resultant spatiotemporal precipitation data. The first EOF (EOF1, Figure 11), which explains 77.71% of the total annual climatological cycle precipitation variance, shows higher precipitation along the Pacific coast and Yucatán Peninsula, and relatively low

precipitation in southern Mexico and Cuba. The pattern of EOF1 is similar to the climatological precipitation in traditionally defined rainy seasons (May to October) over Central America and Mexico (e.g., Zhao et al., 2020), implying that EOF1 is a useful measure of the characteristic climatological precipitation variability across the region. Characterized by an obvious bimodal shape, PC1 demonstrates the annual bimodal precipitation over Central America and Mexico, which is scaled regionally across the spatial domain by the EOF1 loadings. the rainy season in this study is hence determined as the period when $PC1 > 0$ (May 17th to October 27th). This determined rainy season is used throughout this section.

Smoothed using a 31–day moving-average window, the seasonal varying climatology of precipitation during the rainy season at each grid point across the domain is modelled using a fourth-order polynomial:

$$P \sim b_0 + b_1 \times t + b_2 \times t^2 + b_3 \times t^3 + b_4 \times t^4$$

where P indicates the precipitation time series at each grid point during the rainy season, $b_0 - b_4$ correspond to the fitted coefficients for each polynomial term, and t indicates the corresponding time (day). The application of the fourth-order polynomial here is due to the fact that it gives the best modelling outputs, while polynomials of smaller order (e.g., third-order) generate lower R^2 and higher order polynomials (fifth-order or above) induce overfitting problems shown by a generally insignificant coefficient on the largest order term (not shown here). In this study, we focus on analyzing the coefficient of fourth-order polynomial term, b_4 , which is the key factor to determine the polynomial shape of the fitted model. The resultant R^2 and coefficient b_4 are shown in Figure 12, with determined MSD areas indicated by the stippling. In most areas of the domain, the polynomial generates satisfying modelling outputs for the rainy season precipitation, shown by generally high R^2 (~ 0.8) across much of the domain. It is notable that R^2 is still reasonable ($R^2 > 0.5$) even in those regions where the performance is the weakest, such as the coasts around the Gulf of Mexico and Panama. Overall, we find that the performance of b_4 varies with the strength of the bimodal precipitation. In areas exhibiting MSD signals, b_4 is generally negative and statistically significant (at the 95% level), whereas it tends to be insignificant or significantly positive in non–MSD characterized areas. The tendency is clearer after the climatological precipitation is spatially averaged based on the performance of b_4 (Figure 13). The bimodal annual cycle of precipitation is evident in areas characterized by significantly negative b_4 , while precipitation in other regions b_4 tends to be dominated by a unimodal precipitation annual cycle.

The performance of the aforementioned method proves to be unsatisfactory when applied to the daily precipitation time series in the rainy season over the 1979 – 2017 period. The polynomial is applied to rainy season precipitation for every single year in each grid and the resultant b_4 and R^2 are temporally averaged (Figure 14). It is notable that, while the temporally averaged b_4 generally follows the pattern shown in Figure 12, the spatial R^2 drops significantly (< 0.5 in a large part of the domain). It indicates that the fourth-order polynomial model fails to reveal some interannual variations of the intraseasonal variability, which may be filtered during the calculation of seasonally varying climatology.

To reveal these unresolved intraseasonal variabilities, the polynomial model is modified by adding the MJO indexes:

$$P \sim b_0 + b_1 \times t + b_2 \times t^2 + b_3 \times t^3 + b_4 \times t^4 + a_1 \times RMM1 + a_2 \times RMM2$$

The updated model, with MJO covariates, is applied to the precipitation time series during the rainy season for every year and grid point over the domain. After temporally averaging, the resultant R^2 , b_4 and regression coefficients on the MJO covariates (a_1 and a_2) are shown in Figure 15. Although the R^2 magnitudes (Figure 15a) are not as large as the climatological values (cf. Figure 12), it clearly increases after adding the MJO indexes, implying that the inclusion of the MJO makes an important contribution to addressing the previously unresolved variability across the region. The temporally averaged b_4 is similar to the previous one for the climatological (Figure 12) and daily (Figure 14) analyses, indicating that the added covariates (MJO indexes) do not disturb the performance of the other polynomial terms. This implies that the added covariates are generally orthogonal to the polynomial terms. The widespread statistical significances of the a_1 and a_2 coefficients over the domain imply that the inclusion of the MJO indexes add considerable value to the model's explanation of the overall variability, with relatively little effects of overfitting or overdispersion. It is notable that a_1 and a_2 are significantly negative in most characteristic MSD regions, while they tend to be positive or insignificant in characteristically non-MSD regions. Based on the RMM1 – RMM2 phases (phases 1 – 8), the performance of a_1 and a_2 can be interpreted as the phase-shifting of the MJO. The increase of RMM1 and RMM2 together contributes to the phase shifting from MJO phase 2 to 5, corresponding to a period of precipitation reduction in the rainy season. Similarly, the decrease of RMM1 and RMM2 corresponds to the phase shifting from phase 6 to phase 1 and associated rainfall enhancement in the rainy season.

Based on the results shown above, the bimodal precipitation during the rainy seasons in the MSD characterized regions can be synoptically explained by a fourth-order bimodal signature and the modulation through two complete MJO cycles (Figure 16). Over characteristic MSD regions, the rainy season starts with a rapid increase in precipitation during MJO phase 5/6 to 8/1. After reaching the first precipitation peak, the subsequent precipitation reduction (into the MSD trough) typically exists from late June/early July through to late August/early September, characterized by a full MJO cycle. Following the end of the MSD period, precipitation tends to rapidly decrease again through the next month, transitioning into the dry season. This coincides with a shift of the MJO from phases 8–1 to 5–6.

4 Discussion

4.1 Spatial and temporal variabilities

In this study, we detected MSD signals over Central America and Mexico using daily time-scale data over the period from 1979 to 2017. We found that large parts of southern Mexico and Central America display

constant and frequent MSD signatures, characterized by significant spatial and temporal variability. The detected MSD signals tend to have longer durations and wide temporal ranges, characterized by earlier onset and later end date, towards the southeast. Several regions exhibit strong MSD signatures, including the Pacific Coast of Central America, Cuba and the Gulf of Mexico. The spatial patterns of detected MSD signals are generally similar to those shown by Zhao et al. (2020), using the same dataset from 1993 to 2017, except for some minor biases in the central region of the Yucatán Peninsula. The pattern similarity highlights the temporal length of the data we used is sufficient to simulate the climatological signature of MSD mean states, it also supports the robustness of the method. The temporal variability of the MSD signals is characterized by complex, noisy and no-autocorrelated signatures. This implies that the frequency of the MSD signals over the domain does not have a significant trend over the period 1979 – 2017.

The large scale composites of climate properties are used to dynamically illustrate the development of MSD signals, including onset, peak and end dates. The most important and interesting signature found is the change of the wind–pressure system relationship for different MSD periods. Specifically, we found that there are characteristically cyclonic anomalies for periods with higher precipitation (onset, end dates) and anticyclonic anomalies for periods with lower precipitation (peak date). During the onset/end of MSD signals, the near–surface temperature (2m temperature and SST) anomalies over the domain is generally negative, while positive temperature anomalies exist during the peak date.

Magaña et al. (1999) pointed out the warming and cooling of the eastern Pacific Ocean could be a significant contributor to the bimodal signature of precipitation for Central America and Mexico. According to their theory, the warming eastern Pacific could induce active upward convection and corresponding intense precipitation (during the onset/end of the MSD), while oceanic cooling corresponds to the reduction of precipitation (during the peak of the MSD). However, this signature is not evident in near–surface temperature composites in the present study, which is characterized by anomalously low temperatures during the onset/end of MSD signals and anomalously warm temperatures during the peak of MSD. This bias could be due to the examination of anomalies instead of raw SST to calculate the composites in the present study. Magaña et al. (1999) used absolute SST to characterize the change of heat content during the development of the MSD, which highlights the contribution of SST warming and cooling, while the examination of anomalies in this study focuses on the influence from near–surface wind circulations. Mechanisms proposed in previous studies (e.g., Magaña et al., 1999, Karnauskas et al., 2013, Perdigón-Morales et al., 2021) indicate that the generation of the MSD is not induced by a single factor, but rather a combination of multiple physical factors including sea–air–coast interactions and large–scale climate modes. The application of realistic and idealized climate models, which enable the removal of some physical properties, may more clearly reveal the mechanisms behind the MSD.

4.2 Connections with climate modes and associated predictability

The relationship found between MSD metrics and the ONI suggests that longer MSDs tend to be stronger and may be enhanced by El Niño and suppressed by La Niña. The positive ENSO phase (El Niño) can suppress precipitation during boreal summer and strengthen the North Atlantic Subtropical High (NASH) and its associated easterlies from the Caribbean region, which can intensify the MSD and potentially extend the MSD duration. The easterlies, which are significantly contributed to by the peak of the Caribbean Low – Level Jet (CLLJ) can potentially modulate the MSD through two different processes: the strengthened easterlies suppress the convection, especially during the peak to the end dates of the MSD, inducing a drier and subsequently more intense MSD period, on the other hand, the interaction between the coastal wind and steep topography can also contribute to the change of precipitation, since positive ENSO phases can bring easterly anomalies, which are offshore winds on the Pacific side of Central America and Mexico. These offshore winds can suppress the orographic uplifting, and subsequently reduce the rainfall in these regions.

ENSO's influence on MSDs is controversial. Many studies argue that positive ENSO phases strengthen the MSD (Chen and Taylor, 2002, Curtis, 2002, Hidalgo et al., 2017, Díaz-Esteban and Raga, 2018) while others suggest that the MSD signal may be weaker during El Niño years (Magaña et al., 1999, 2003, Peralta-Hernández et al., 2008). Our results indicate that ENSO's influence on the MSD is through modulation of the NASH and associated near–surface wind fields. Furthermore, this corresponds to observations of an intensified NASH (Giannini et al., 2000) and CLLJ (Wang, 2007, Krishnamurthy et al., 2015), as well as their teleconnection during boreal summer, and highlights the role of the low–level circulation system in the generation of the MSD.

Based on our categorization of the MSD into four periods and their relationship with MJO-phase, we have shown that a relatively high proportion of MSD periods tend to start/end in MJO phase 8–1 due to the anomalous onshore winds arising at the coasts of Central America. This result is consistent with a previous study of MSDs over Costa Rica (Poleo et al., 2014, Zhao et al., 2019) and Mexico (Perdigón-Morales et al., 2019). Additionally, the teleconnection between wind–pressure patterns in MSD P1 and P4 and MJO phases 8–1 have also been identified. The varying wind patterns associated with MJO phases imply that MJO affects precipitation throughout the entirety of MSD signatures, rather than being limited in starting/ending periods.

An important MSD signature investigated in this study is through the fourth-order polynomial regression modelling of the intraseasonal variability, including the phase shifting by the MJO. Overall, we found that the mean states of the rainy season precipitation over the domain were captured well by the model. Specifically, we found that the polynomial coefficient b_4 can be a practical index to quantify the strength of climatological MSDs over the domain. We found that a significantly negative b_4 dominates MSD areas, while non–MSD areas generally exhibit significantly positive or insignificant b_4 . The model was found to perform much worse using annual precipitation data, while the rainy season could be optimized by adding the MJO indexes as covariates in the model, implying that the unresolved intraseasonal variability in each year could be largely covered by changes in MJO phases.

The areas exhibiting climatological MSD signals exhibit generally negative coefficients of MJO-associated covariates. We interpret this as an MJO phase-shifting effect here that significantly influences the characteristic intraseasonal variabilities of precipitation during the rainy season across the MSD area. Changes in MJO phases from phase 5/6 to 8/1 lead to increased precipitation, contributing to the first precipitation peak, corresponding to the onset of the MSD. A complete MJO cycle induces a precipitation reduction, corresponding to the trough of the MSD. Finally, the MJO transitions from phase 8/1 through to 5/6, contributing to a rapid decrease in precipitation, implying the end of the rainy season. The intraseasonal variability of precipitation through the rainy season in the MSD areas is clearly and significantly modulated by the MJO.

In the conceptual model proposed in this study, we used two complete MJO cycles to explain the interannual variability of MSD signals during the rainy seasons. The duration of two complete MJO cycles (~100 days, Zhang, 2005) used in the hypothesis, however, does not critically match the period of rainy season used in this study, which is from May 17th to October 27th (164 days). This bias can be caused by several factors. Firstly, the MJO phases in Julian days of year vary annually, implying the MJO's modulation on intraseasonal precipitation varies interannually. Secondly, while the addition of MJO indexes in the regression model provides considerable improvement, ~20% of the total variance remains unresolved, which may be due to other large-scale climate modes such as ENSO and/or the Interdecadal Pacific Oscillation, and regional forcing such as diabatic heating (Vincent and Lane, 2018).

The implication of the MJO on regional circulation, shown by the changing wind-pressure system associated with changes in MJO phase, could largely contribute to the generation and maintenance of the bimodal precipitation signature (including the so-called 'mid-summer drought') through the rainy season. We have found that a fourth-order polynomial regression model captures a large proportion of the precipitation variability, indicating the potential predictability of the bimodal precipitation signature. Several MJO modelling approaches, including a damped harmonic oscillator model (Oliver and Thompson, 2016), linear inverse model (Cavanaugh et al., 2015), ensemble general circulation models (Seo et al., 2009, Vitart, 2014) and atmosphere-ocean coupled models, have been shown to capture MJO predictability and offer the potential to predict MJO dynamically, mathematically or statistically with lead times <4 weeks (Waliser et al., 2006). Considering the wide use and constant development of MJO indexes (e.g. Wheeler and Hendon, 2004, Liu et al., 2016, Mansouri et al., 2021), skillful prediction of MJO events and their transition phases are likely to play a key role in potentially improving the predictability of MSD events.

Declarations

Acknowledgements

NJH acknowledges support from the ARC Centre of Excellence for Climate Extremes (CE17010023).

Code Availability Statement

Most codes used to generate results in this study are publicly available via https://github.com/ZijieZhaoMMHW/MSD_Signatures. Other codes are available from the corresponding author.

References

1. Amador, J.A., 2008. The intra-Americas sea low-level jet: Overview and future research. *Annals of the New York Academy of Sciences*, 1146(1), pp.153-188.
2. Amador, J.A., Alfaro, E.J., Lizano, O.G. and Magaña, V.O., 2006. Atmospheric forcing of the eastern tropical Pacific: A review. *Progress in Oceanography*, 69(2-4), pp.101-142.
3. Ashby, S.A., Taylor, M.A. and Chen, A.A., 2005. Statistical models for predicting rainfall in the Caribbean. *Theoretical and Applied Climatology*, 82(1), pp.65-80.
4. Cavanaugh, N.R., Allen, T., Subramanian, A., Mapes, B., Seo, H. and Miller, A.J., 2015. The skill of atmospheric linear inverse models in hindcasting the Madden–Julian Oscillation. *Climate dynamics*, 44(3-4), pp.897-906.
5. Chen, A.A. and Taylor, M.A., 2002. Investigating the link between early season Caribbean rainfall and the El Niño+ 1 year. *International Journal of Climatology: A Journal of the Royal Meteorological Society*, 22(1), pp.87-106.
6. Chen, M., Shi, W., Xie, P., Silva, V.B., Kousky, V.E., Wayne Higgins, R. and Janowiak, J.E., 2008. Assessing objective techniques for gauge-based analyses of global daily precipitation. *Journal of Geophysical Research: Atmospheres*, 113(D4).
7. Corrales-Suastegui, A., Fuentes-Franco, R. and Pavia, E.G., 2020. The mid-summer drought over Mexico and Central America in the 21st century. *International Journal of Climatology*, 40(3), pp.1703-1715.
8. Curtis, S. and Gamble, D.W., 2008. Regional variations of the Caribbean mid-summer drought. *Theoretical and Applied Climatology*, 94(1), pp.25-34.
9. Curtis, S., 2002. Interannual variability of the bimodal distribution of summertime rainfall over Central America and tropical storm activity in the far-eastern Pacific. *Climate Research*, 22(2), pp.141-146.
10. Daly, C., 2002. Variable influence of terrain on precipitation patterns: Delineation and use of effective terrain height in PRISM. *Oregon State University*.
11. Daly, C., Neilson, R.P. and Phillips, D.L., 1994. A statistical-topographic model for mapping climatological precipitation over mountainous terrain. *Journal of applied meteorology*, 33(2), pp.140-158.
12. Dee, D.P., Uppala, S.M., Simmons, A.J., Berrisford, P., Poli, P., Kobayashi, S., Andrae, U., Balmaseda, M.A., Balsamo, G., Bauer, D.P. and Bechtold, P., 2011. The ERA-Interim reanalysis: Configuration and performance of the data assimilation system. *Quarterly Journal of the royal meteorological society*, 137(656), pp.553-597.

13. Díaz, D.P., Córdova, Q.A. and Grayeb, B.E.P., 1994. Effect on ENSO on the mid-summer drought in Veracruz State, Mexico. *Atmósfera*, 7(4), pp.211-219.
14. Díaz-Esteban, Y. and Raga, G.B., 2018. Weather regimes associated with summer rainfall variability over southern Mexico. *International Journal of Climatology*, 38(1), pp.169-186.
15. Fallas López, B. and Alfaro Martínez, E.J., 2012. Uso de herramientas estadísticas para la predicción estacional del campo de precipitación en América Central como apoyo a los Foros Climáticos Regionales. 1: Análisis de tablas de contingencia.
16. Gamble, D.W., Parnell, D.B. and Curtis, S., 2008. Spatial variability of the Caribbean mid-summer drought and relation to north Atlantic high circulation. *International Journal of Climatology: A Journal of the Royal Meteorological Society*, 28(3), pp.343-350.
17. García-Martínez, I.M. (2015) Variabilidad océano-atmósfera asociada a la sequía intraestival en el reanálisis CFSR. MSc thesis, Baja California, Centro de Investigación Científica y de Educación Superior de Ensenada, 71 pp.
18. García-Martínez, I.M. (2015) Variabilidad océano-atmósfera asociada a la sequía intraestival en el reanálisis CFSR. MSc thesis, Baja California, Centro de Investigación Científica y de Educación Superior de Ensenada, 71 pp.
19. Giannini, A., Kushnir, Y. and Cane, M.A., 2000. Interannual variability of Caribbean rainfall, ENSO, and the Atlantic Ocean. *Journal of Climate*, 13(2), pp.297-311.
20. Hastenrath, S.L., 1967. Rainfall distribution and regime in Central America. *Archiv für Meteorologie, Geophysik und Bioklimatologie, Serie B*, 15(3), pp.201-241.
21. Herrera, E., Magaña, V. and Caetano, E., 2015. Air–sea interactions and dynamical processes associated with the midsummer drought. *International Journal of Climatology*, 35(7), pp.1569-1578.
22. Hou, D., Charles, M., Luo, Y., Toth, Z., Zhu, Y., Krzysztofowicz, R., Lin, Y., Xie, P., Seo, D.J., Pena, M. and Cui, B., 2014. Climatology-calibrated precipitation analysis at fine scales: Statistical adjustment of stage IV toward CPC gauge-based analysis. *Journal of Hydrometeorology*, 15(6), pp.2542-2557.
23. Huang, B., L'Heureux, M., Hu, Z.Z. and Zhang, H.M., 2016. Ranking the strongest ENSO events while incorporating SST uncertainty. *Geophysical Research Letters*, 43(17), pp.9165-9172.
24. Huang, B., Liu, C., Banzon, V., Freeman, E., Graham, G., Hankins, B., Smith, T. and Zhang, H.M., 2021. Improvements of the daily optimum interpolation sea surface temperature (DOISST) version 2.1. *Journal of Climate*, 34(8), pp.2923-2939.
25. Huang, B., Thorne, P.W., Banzon, V.F., Boyer, T., Chepurin, G., Lawrimore, J.H., Menne, M.J., Smith, T.M., Vose, R.S. and Zhang, H., 2017. NOAA Extended Reconstructed Sea Surface Temperature (ERSST), Version 5. *NOAA National Centers for Environmental Information*.
26. Inoue, M., Handoh, I.C. and Bigg, G.R., 2002. Bimodal distribution of tropical cyclogenesis in the Caribbean: Characteristics and environmental factors. *Journal of Climate*, 15(20), pp.2897-2905.
27. Karnauskas, K.B., Seager, R., Giannini, A. and Busalacchi, A.J., 2013. A simple mechanism for the climatological midsummer drought along the Pacific coast of Central America. *Atmósfera*, 26(2), pp.261-281.

28. Katiraie-Boroujerdy, P.S., Nasrollahi, N., Hsu, K.L. and Sorooshian, S., 2013. Evaluation of satellite-based precipitation estimation over Iran. *Journal of arid environments*, 97, pp.205-219.
29. Krishnamurthy, L., Vecchi, G.A., Msadek, R., Wittenberg, A., Delworth, T.L. and Zeng, F., 2015. The seasonality of the Great Plains low-level jet and ENSO relationship. *Journal of Climate*, 28(11), pp.4525-4544.
30. Liebmann, B., Bladé, I., Bond, N.A., Gochis, D., Allured, D. and Bates, G.T., 2008. Characteristics of North American summertime rainfall with emphasis on the monsoon. *Journal of Climate*, 21(6), pp.1277-1294.
31. Liu, P., Zhang, Q., Zhang, C., Zhu, Y., Khairoutdinov, M., Kim, H.M., Schumacher, C. and Zhang, M., 2016. A revised real-time multivariate MJO index. *Monthly Weather Review*, 144(2), pp.627-642.
32. Lorenz, E.N., 1956. Empirical orthogonal functions and statistical weather prediction.
33. Magaña, V. and Caetano, E., 2005. Temporal evolution of summer convective activity over the Americas warm pools. *Geophysical Research Letters*, 32(2).
34. Magaña, V., Amador, J.A. and Medina, S., 1999. The midsummer drought over Mexico and Central America. *Journal of Climate*, 12(6), pp.1577-1588.
35. Maldonado, T., Rutgersson, A., Alfaro, E., Amador, J., and Claremar, B. Interannual variability of the midsummer drought in Central America and the connection with sea surface temperatures, *Adv. Geosci.*, 42, pp. 35–50.
36. Mansouri, S., Masnadi-Shirazi, M.A., Golbahar-Haghighi, S. and Nazemosadat, M.J., 2021. An analogy toward the real-time multivariate MJO index to improve the estimation of the impacts of the MJO on the precipitation variability over Iran in the boreal cold months. *Asia-Pacific Journal of Atmospheric Sciences*, 57(2), pp.207-222.
37. Mapes, B.E., Liu, P. and Buening, N., 2005. Indian monsoon onset and the Americas midsummer drought: Out-of-equilibrium responses to smooth seasonal forcing. *Journal of climate*, 18(7), pp.1109-1115.
38. Martin, E.R. and Schumacher, C., 2011. Modulation of Caribbean precipitation by the Madden–Julian oscillation. *Journal of Climate*, 24(3), pp.813-824.
39. McCabe, G.J. and Muller, R.A., 2002. Effects of ENSO on weather-type frequencies and properties at New Orleans, Louisiana, USA. *Climate Research*, 20(2), pp.95-105.
40. Mestas-Nuñez, A.M., Enfield, D.B. and Zhang, C., 2007. Water vapor fluxes over the Intra-Americas Sea: Seasonal and interannual variability and associations with rainfall. *Journal of Climate*, 20(9), pp.1910-1922.
41. Mosiño, P. and García, E., 1966. The midsummer droughts in Mexico. In *Proc. Regional Latin American Conf* (Vol. 3, pp. 500-516).
42. Oliver, E.C. and Holbrook, N.J., 2018. Variability and Long-Term Trends in the Shelf Circulation Off Eastern Tasmania. *Journal of Geophysical Research: Oceans*, 123(10), pp.7366-7381.

43. Oliver, E.C. and Thompson, K.R., 2011. A reconstruction of Madden–Julian Oscillation variability from 1905 to 2008. *Journal of Climate*, 25(6), pp.1996-2019.
44. Oliver, E.C. and Thompson, K.R., 2016. Predictability of the Madden–Julian Oscillation index: seasonality and dependence on MJO phase. *Climate Dynamics*, 46(1-2), pp.159-176.
45. Oliver, E.C., Lago, V., Hobday, A.J., Holbrook, N.J., Ling, S.D. and Mundy, C.N., 2018. Marine heatwaves off eastern Tasmania: Trends, interannual variability, and predictability. *Progress in oceanography*, 161, pp.116-130.
46. Peralta-Hernández, A.R., Barba-Martínez, L.R., Magaña-Rueda, V.O., Matthias, A.D. and Luna-Ruíz, J.J., 2008. Temporal and spatial behavior of temperature and precipitation during the canícula (midsummer drought) under El Niño conditions in central México. *Atmósfera*, 21(3), pp.265-280.
47. Perdigón-Morales, J., Romero-Centeno, R., Barrett, B.S. and Ordoñez, P., 2019. Intraseasonal Variability of Summer Precipitation in Mexico: MJO Influence on the Midsummer Drought. *Journal of Climate*, 32(8), pp.2313-2327.
48. Perdigón-Morales, J., Romero-Centeno, R., Ordoñez, P., Nieto, R., Gimeno, L. and Barrett, B.S., 2021. Influence of the Madden-Julian Oscillation on moisture transport by the Caribbean Low Level Jet during the Midsummer Drought in Mexico. *Atmospheric Research*, 248, p.105243.
49. Perdigón-Morales, J., Romero-Centeno, R., Pérez, P.O. and Barrett, B.S., 2018. The midsummer drought in Mexico: perspectives on duration and intensity from the CHIRPS precipitation database. *International Journal of Climatology*, 38(5), pp.2174-2186.
50. Poleo, D., Solano-León, E.Y. and Stolz, W., 2014. La Oscilación atmosférica Madden-Julian (MJO) y las lluvias en Costa Rica. *Tópicos Meteorológicos y Oceanográficos*, 13, 58.
51. Portig, W.H., 1961. Some climatological data of Salvador, Central America. *Weather*, 16(4), pp.103-112.
52. Preethi, B., Revadekar, J.V. and Munot, A.A., 2011. Extremes in summer monsoon precipitation over India during 2001–2009 using CPC high-resolution data. *International journal of remote sensing*, 32(3), pp.717-735.
53. Rana, S., McGregor, J. and Renwick, J., 2015. Precipitation seasonality over the Indian subcontinent: An evaluation of gauge, reanalyses, and satellite retrievals. *Journal of Hydrometeorology*, 16(2), pp.631-651.
54. Rauscher, S.A., Giorgi, F., Diffenbaugh, N.S. and Seth, A., 2008. Extension and intensification of the Meso-American mid-summer drought in the twenty-first century. *Climate Dynamics*, 31(5), pp.551-571.
55. Reynolds, R.W., Smith, T.M., Liu, C., Chelton, D.B., Casey, K.S. and Schlax, M.G., 2007. Daily high-resolution-blended analyses for sea surface temperature. *Journal of climate*, 20(22), pp.5473-5496.
56. Romero-Centeno, R., Zavala-Hidalgo, J., Gallegos, A. and O'Brien, J.J., 2003. Isthmus of Tehuantepec wind climatology and ENSO signal. *Journal of Climate*, 16(15), pp.2628-2639.
57. Romero-Centeno, Rosario, Jorge Zavala-Hidalgo, and G. B. Raga. "Midsummer gap winds and low-level circulation over the eastern tropical Pacific." *Journal of Climate* 20, no. 15 (2007): 3768-3784.

58. Seo, K.H., Wang, W., Gottschalck, J., Zhang, Q., Schemm, J.K.E., Higgins, W.R. and Kumar, A., 2009. Evaluation of MJO forecast skill from several statistical and dynamical forecast models. *Journal of Climate*, 22(9), pp.2372-2388.
59. Small, R.J.O., De Szoeki, S.P. and Xie, S.P., 2007. The Central American midsummer drought: regional aspects and large-scale forcing. *Journal of Climate*, 20(19), pp.4853-4873.
60. Spence, J.M., Taylor, M.A. and Chen, A.A., 2004. The effect of concurrent sea-surface temperature anomalies in the tropical Pacific and Atlantic on Caribbean rainfall. *International Journal of Climatology: A Journal of the Royal Meteorological Society*, 24(12), pp.1531-1541.
61. Taylor, M.A. and Alfaro, E.J., 2005. Climate of central america and the caribbean. *The encyclopedia of world climatology*, pp.183-189.
62. Taylor, M.A., Enfield, D.B. and Chen, A.A., 2002. Influence of the tropical Atlantic versus the tropical Pacific on Caribbean rainfall. *Journal of Geophysical Research: Oceans*, 107(C9), pp.10-1.
63. Ubilava, D. and Helmers, C.G., 2013. Forecasting ENSO with a smooth transition autoregressive model. *Environmental modelling & software*, 40, pp.181-190.
64. Vincent, C.L. and Lane, T.P., 2018. Mesoscale Variation in Diabatic Heating around Sumatra, and Its Modulation with the Madden–Julian Oscillation. *Monthly Weather Review*, 146(8), pp.2599-2614.
65. Vitart, F., 2014. Evolution of ECMWF sub-seasonal forecast skill scores. *Quarterly Journal of the Royal Meteorological Society*, 140(683), pp.1889-1899.
66. Waliser, D., Weickmann, K., Dole, R., Schubert, S., Alves, O., Jones, C., Newman, M., Pan, H.L., Roubicek, A., Saha, S. and Smith, C., 2006. The experimental MJO prediction project. *Bulletin of the American Meteorological Society*, 87(4), pp.425-431.
67. Wang, C., Lee, S.K. and Enfield, D.B., 2007. Impact of the Atlantic warm pool on the summer climate of the Western Hemisphere. *Journal of Climate*, 20(20), pp.5021-5040.
68. Wang, C., Lee, S.K. and Enfield, D.B., 2008. Climate response to anomalously large and small Atlantic warm pools during the summer. *Journal of climate*, 21(11), pp.2437-2450.
69. Wheeler, M.C. and Hendon, H.H., 2004. An all-season real-time multivariate MJO index: Development of an index for monitoring and prediction. *Monthly Weather Review*, 132(8), pp.1917-1932.
70. Xie, P., Yatagai, A., Chen, M., Hayasaka, T., Fukushima, Y., Liu, C. and Yang, S., 2007. A gauge-based analysis of daily precipitation over East Asia. *Journal of Hydrometeorology*, 8(3), pp.607-626.
71. Xie, S.P., Okumura, Y., Miyama, T. and Timmermann, A., 2008. Influences of Atlantic climate change on the tropical Pacific via the Central American Isthmus. *Journal of Climate*, 21(15), pp.3914-3928.
72. Zhang, Y., Wallace, J.M. and Battisti, D.S., 1997. ENSO-like interdecadal variability: 1900–93. *Journal of climate*, 10(5), pp.1004-1020.
73. Zhao, Z., Holbrook, N.J., Oliver, E.C., Ballesterio, D. and Vargas-Hernandez, J.M., 2020. Characteristic atmospheric states during mid-summer droughts over Central America and Mexico. *Climate Dynamics*, 55(3), pp.681-701.

74. Zhao, Z., Oliver, E.C., Ballester, D., Mauro Vargas-Hernandez, J. and Holbrook, N.J., 2019. Influence of the Madden–Julian oscillation on Costa Rican mid-summer drought timing. *International Journal of Climatology*, 39(1), pp.292-301.

Figures

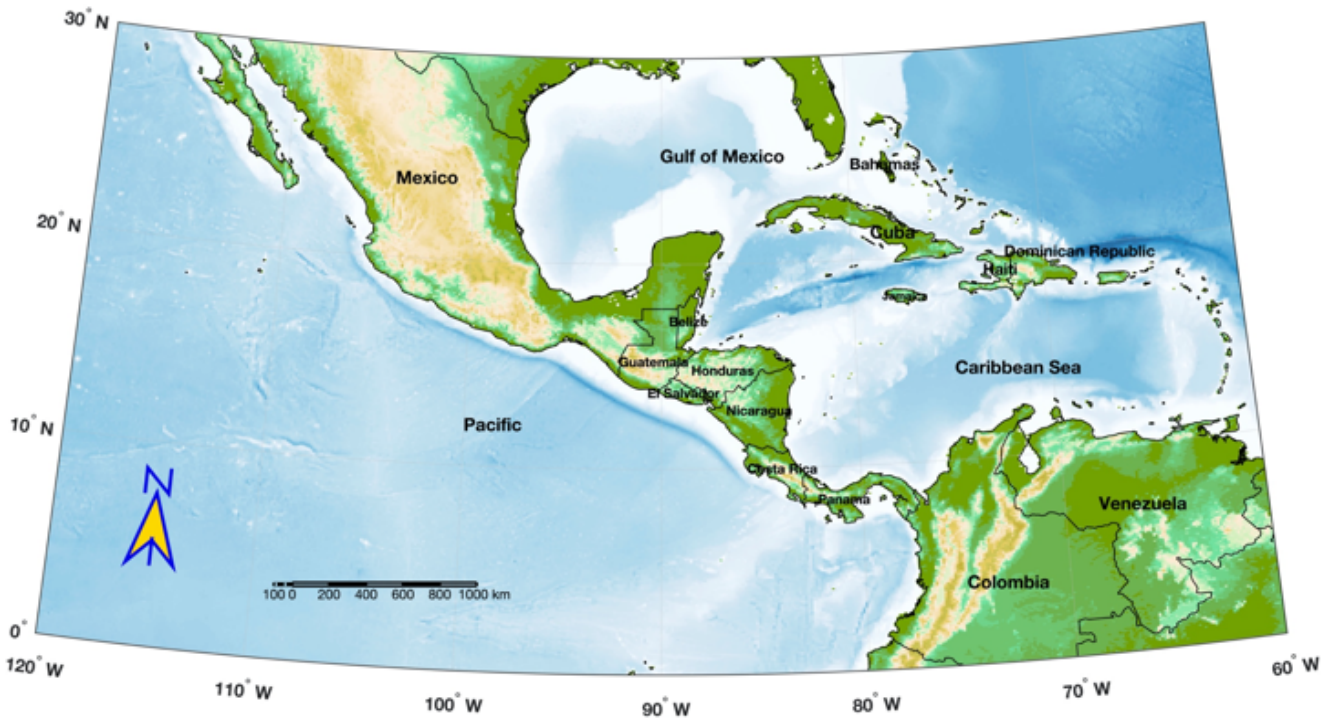


Figure 1

Domain and Bathymetry in this study, including southern Mexico, Central America, northern South America, eastern Pacific, and parts of North Atlantic.

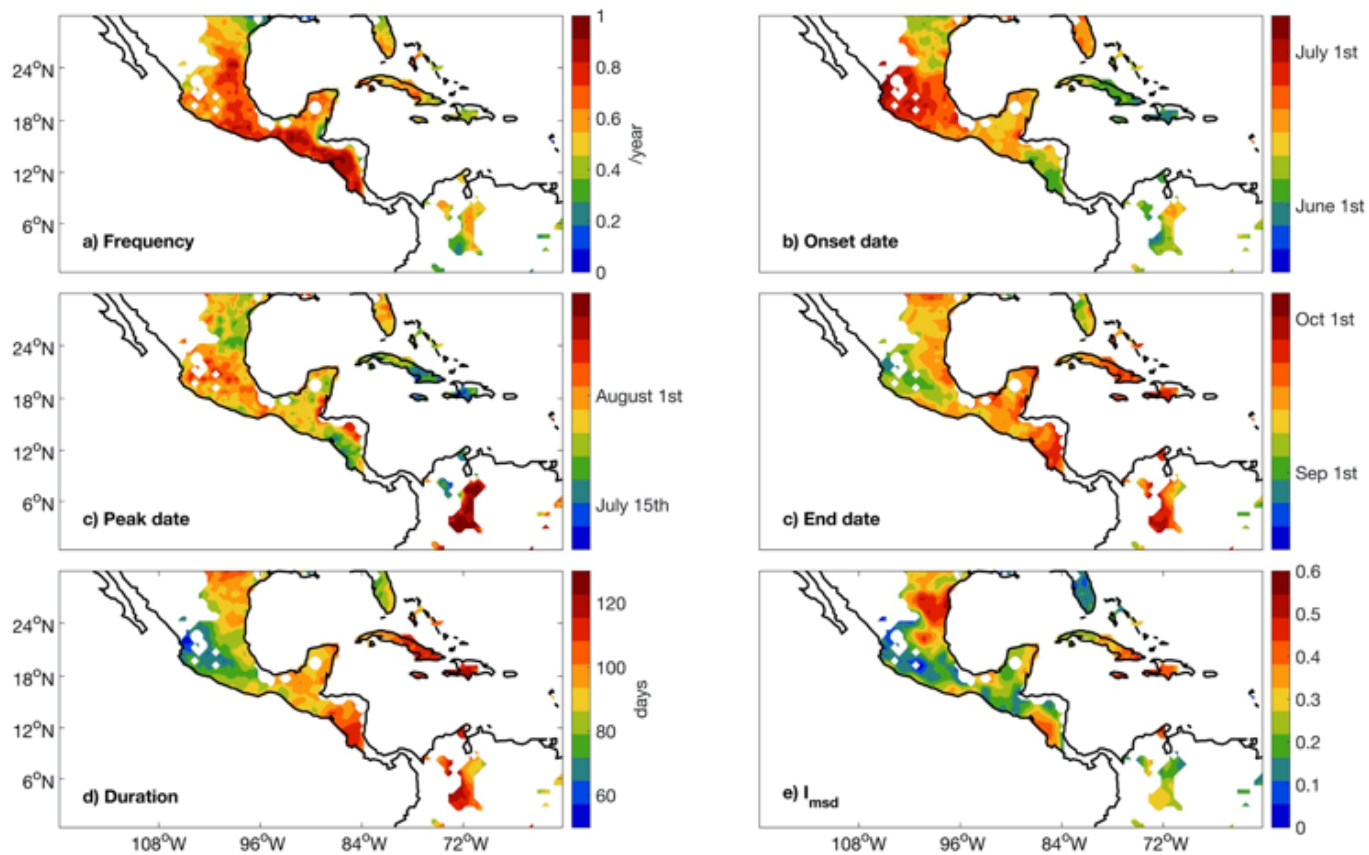


Figure 2

Metrics of MSD signatures over lands of Central America and Mexico. Five panels separately indicate (a) annual frequency, (b) average Julian onset, (c) peak and (d) end dates, (e) average durations and (f) climatological I_{msd} . Regions exhibiting MSD signatures are shaded by colours.

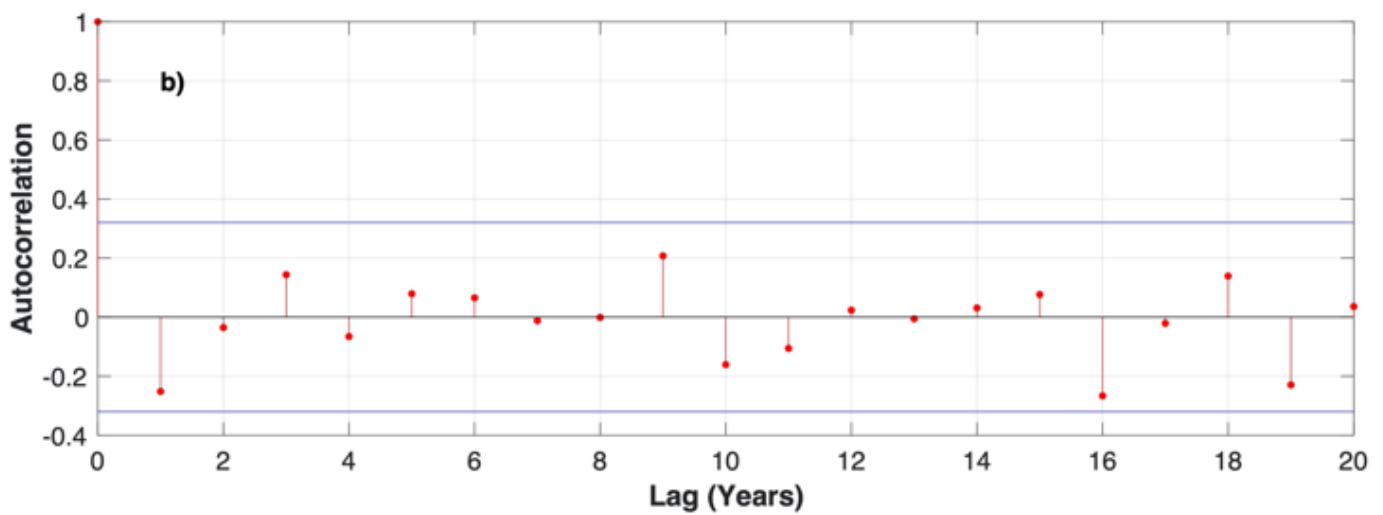
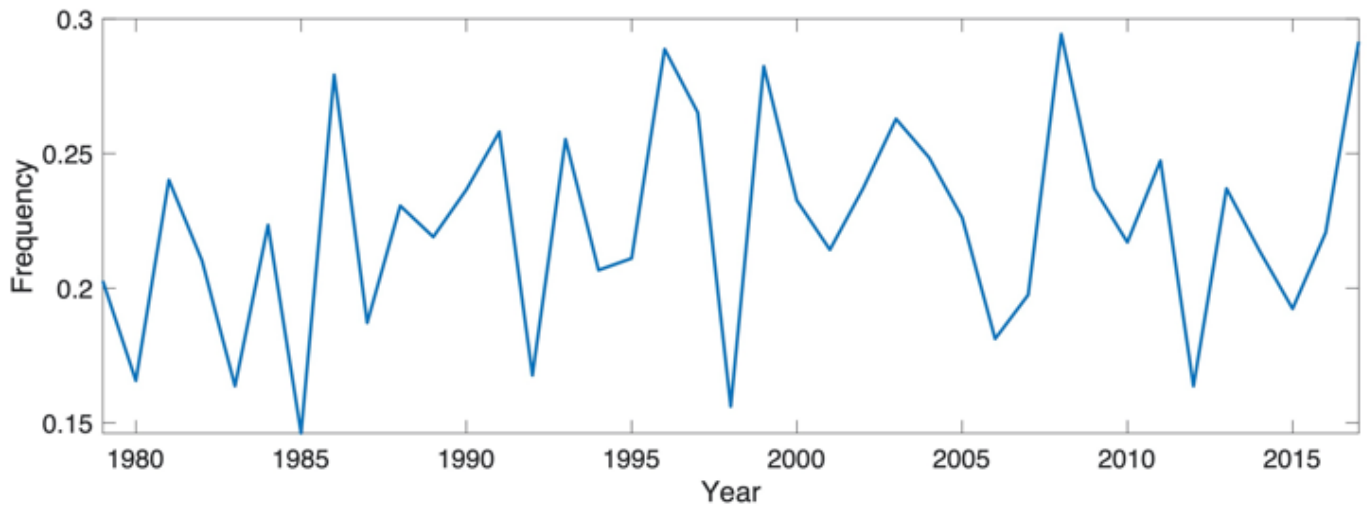


Figure 3

Total number of MSD events in each year and its autocorrelation. (a) The time series of annual number of detected MSD signals summed over the whole domain. (b) The autocorrelation of time series in (a) in varying lags, the statistical significance in 95% level is indicated by blue line.

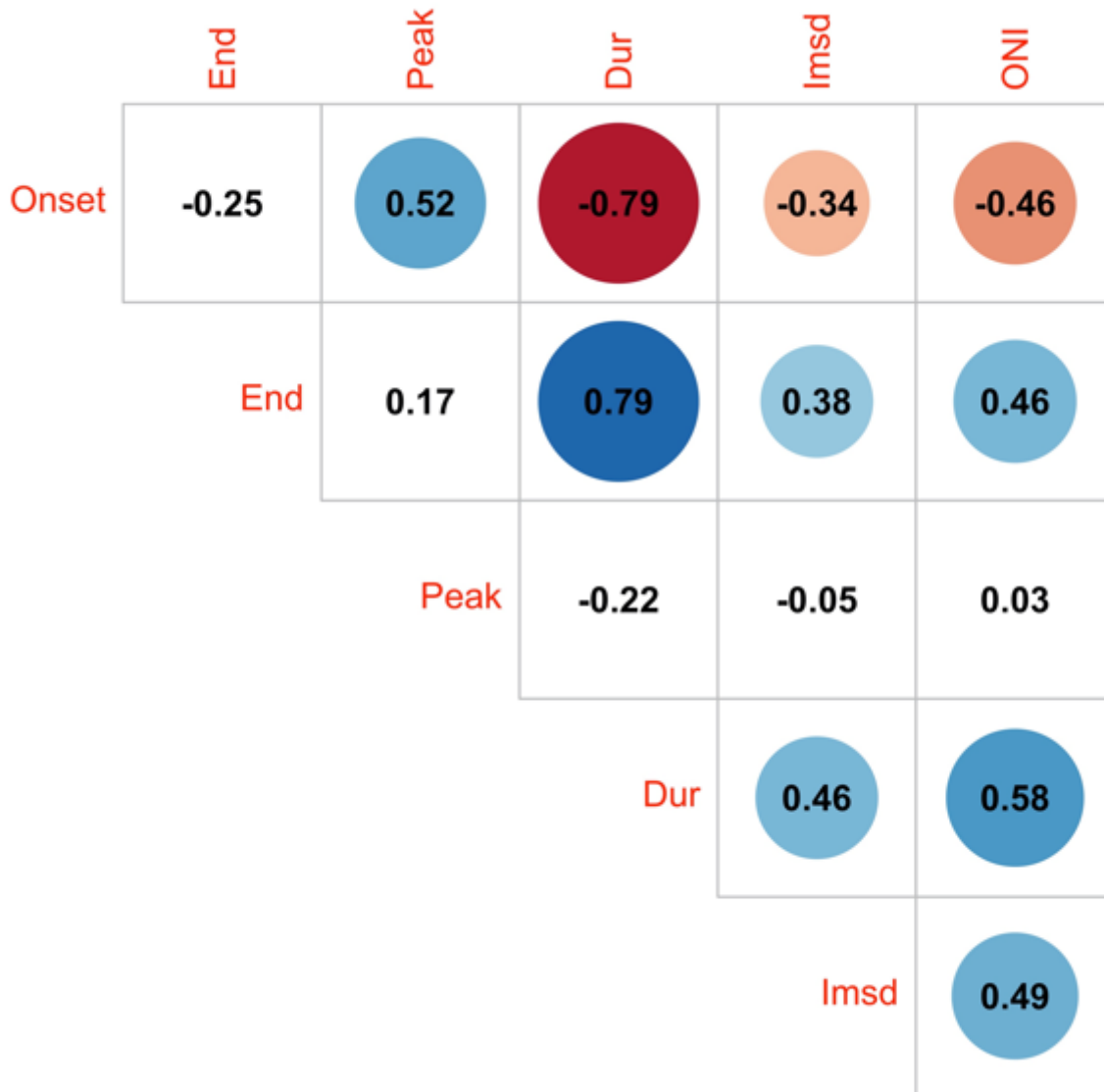


Figure 4

Cross correlation among metrics of MSD signals, including onset, end, and peak dates, durations and I_{msd} , and ONI index. The strength of red (blue) indicates negative (positive) correlation, in 95% statistical significance level.

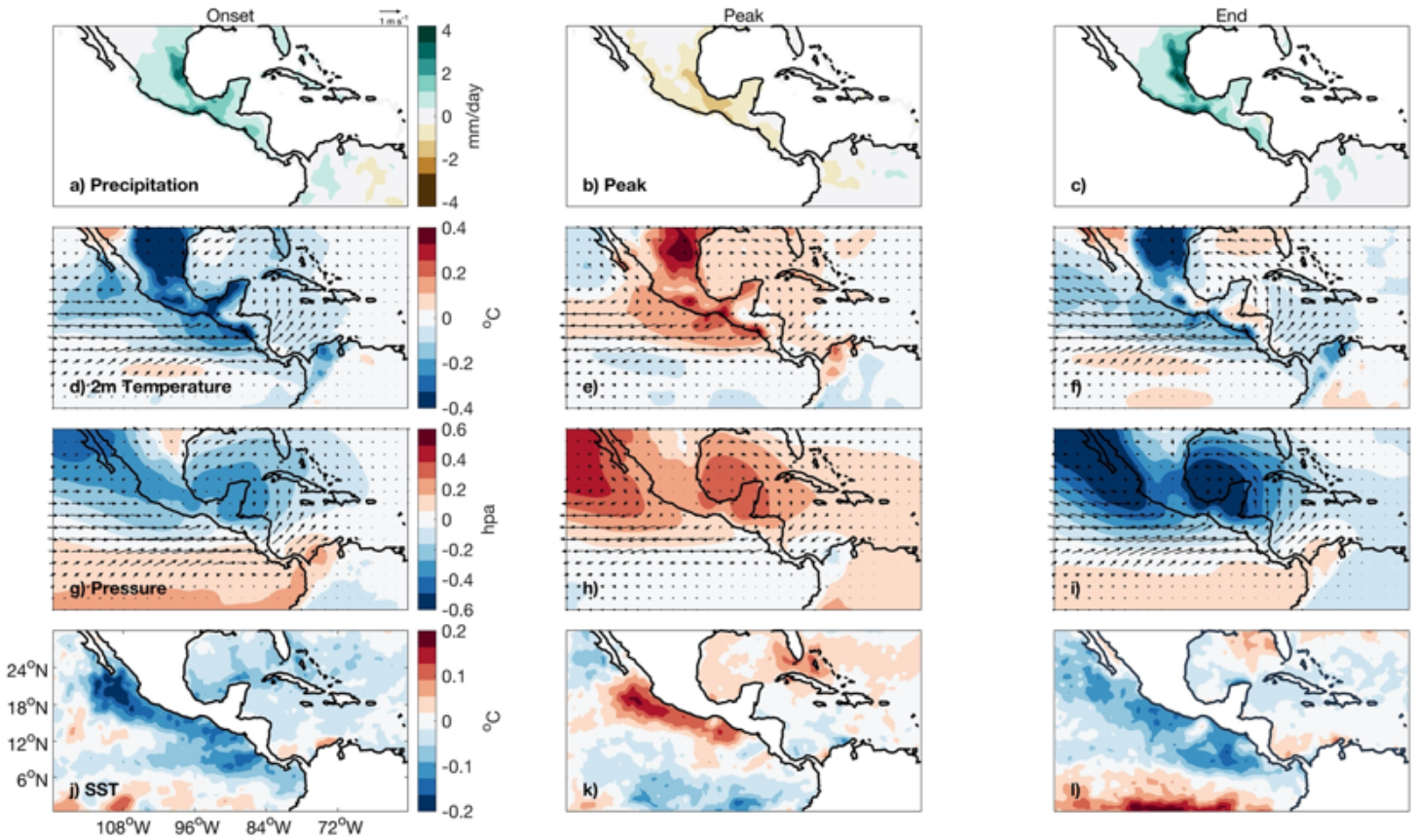


Figure 5

Climate composites in typical time points of MSD. Each column indicates composites in a particular MSD period (onset, peak and end dates), while each row represents a particular atmospheric property (anomalous of precipitation, 2m temperature, 10m horizontal winds, surface pressure and sea surface temperature).

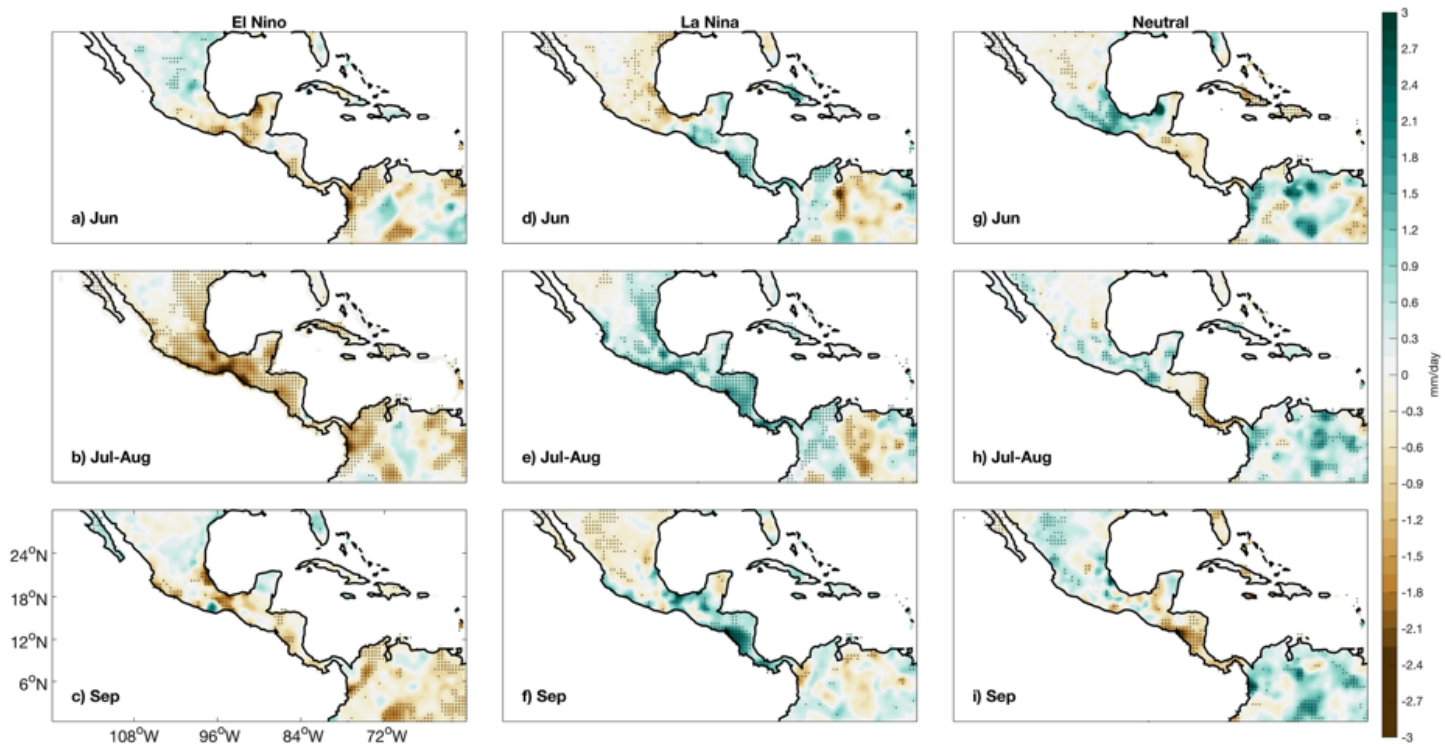


Figure 6

Climatological precipitation across June to September in different ENSO phases. Each row indicates a particular period for climatological precipitation (June, July – August and September), while each column indicates a particular ENSO phase (El Niño, La Niña and neutral years). Dots here indicate statistical significance in 95% confidence intervals.

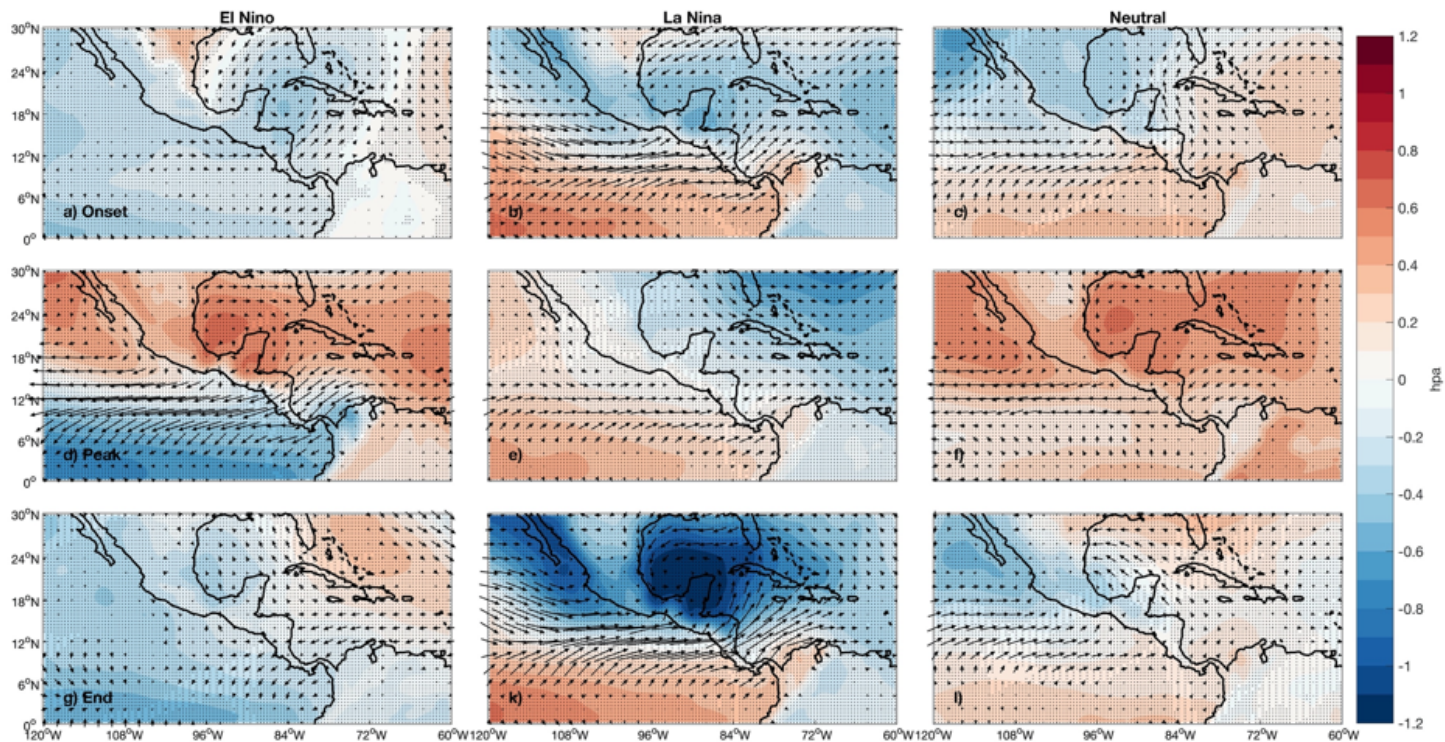


Figure 7

Composites of 10m horizontal winds and surface pressure across all detected MSD events in different ENSO phases. Each row indicates a particular time point in MSD signals (onset, peak and end dates of MSD signals), while each column indicates a particular ENSO phase (El Niño, La Niña and neutral years). Dots here indicate statistical significance in 95% confidence intervals

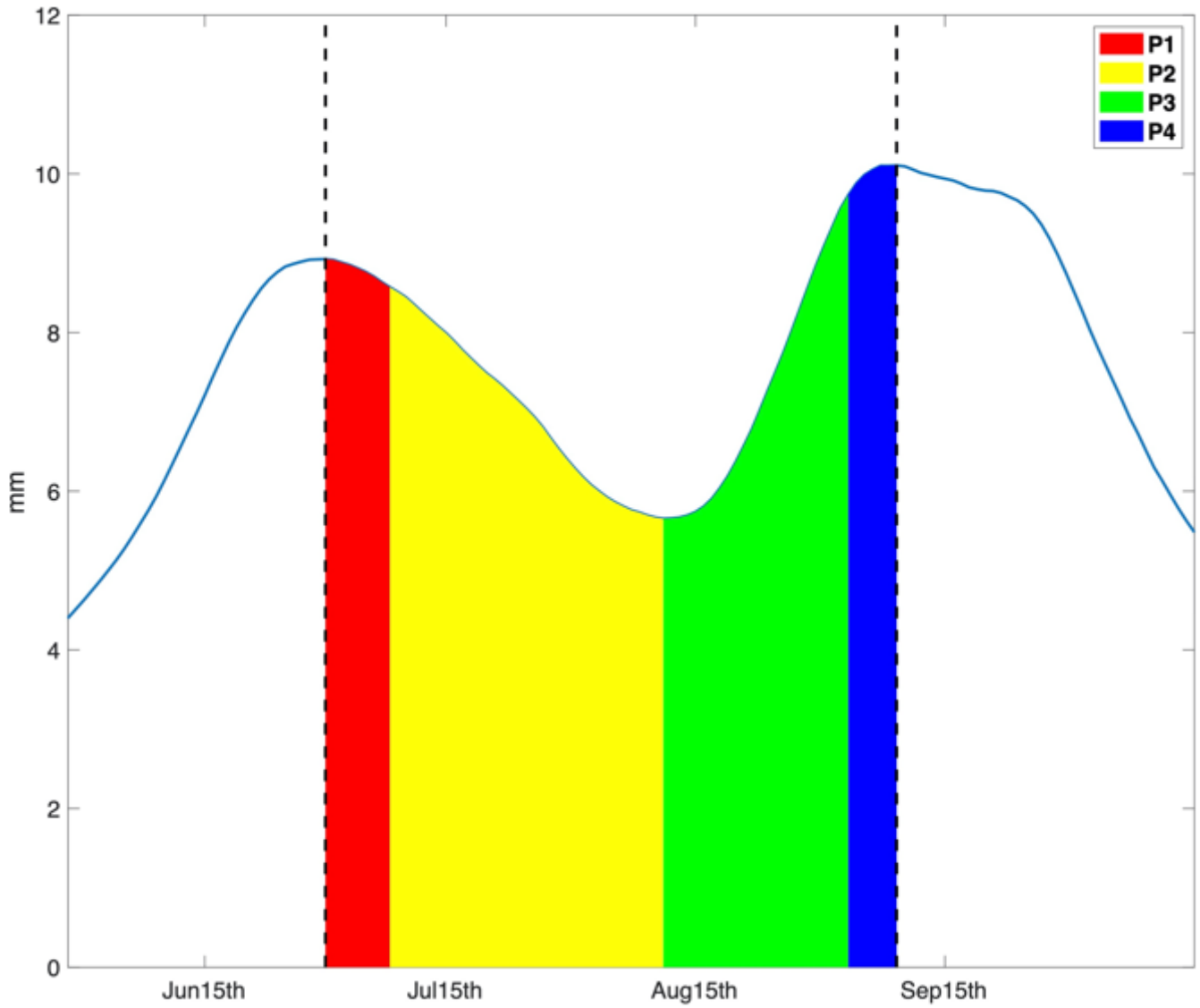


Figure 8

The synoptic illustration for the category of MSD signals. The blue solid line indicates the precipitation, the part of which between the two black vertical dashed line refers to a MSD signal. Four categorized periods, termed as P1 – 4 separately, are distinguished by different colors.

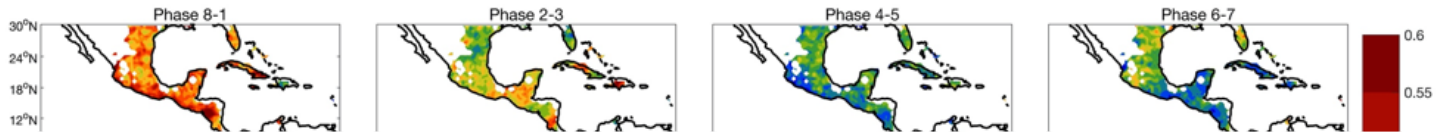


Figure 9

Temporal cooccurrences between MSD periods and MJO phases. Each row indicates a particular MSD period (P1 – 4), while each column indicates a particular segment of MJO phases (8 – 1, 2 – 3, 4- 5, 6- 7). Colours here indicate the proportion of MSD periods in corresponding MJO phases.



Figure 10

Composites of 10m horizontal winds and surface pressure in varying MJO phases. Dots here indicate statistical significance in 95% confidence intervals

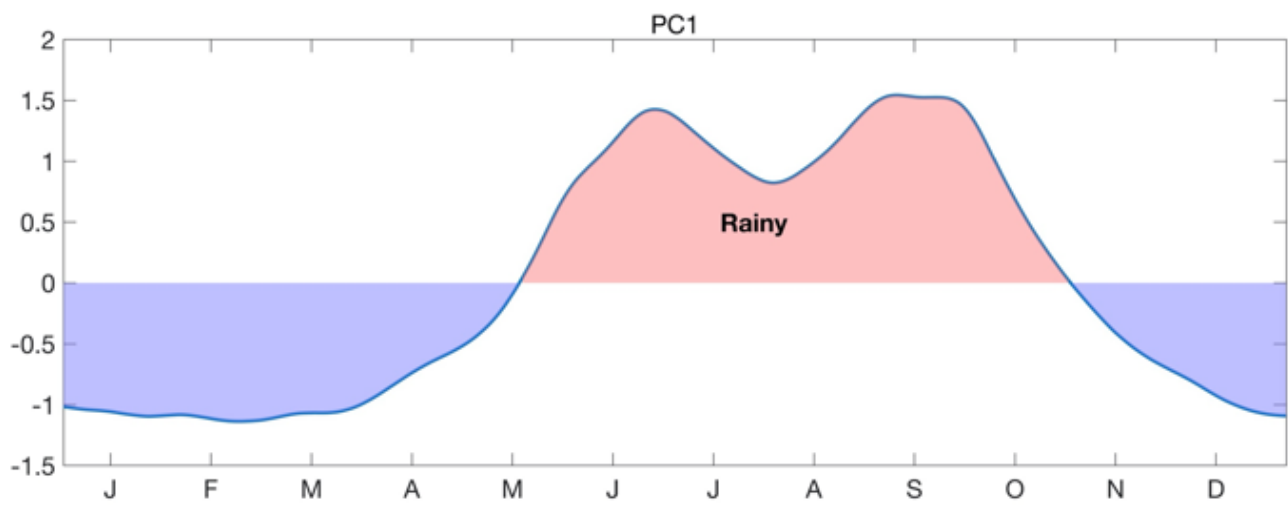
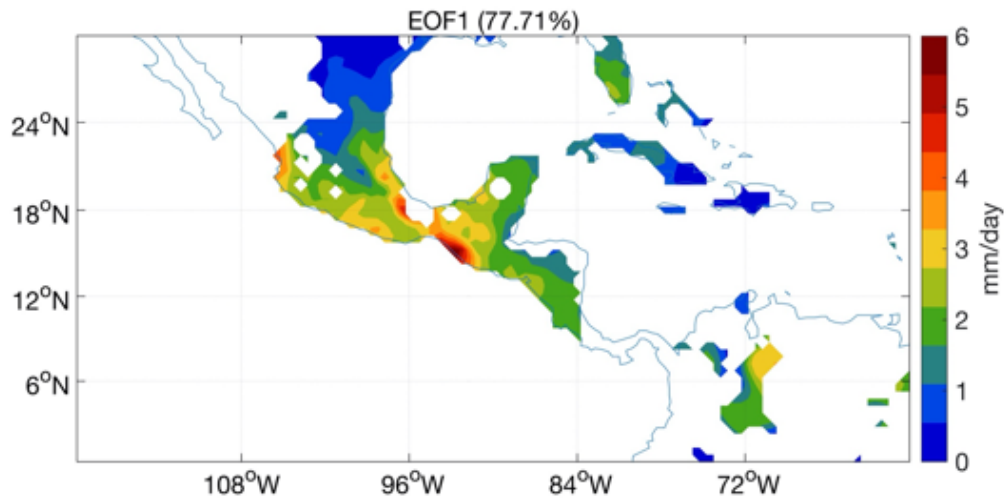


Figure 11

Resultant EOF1 spatial patterns (upper panel) and associated PC1 time series (lower panel).

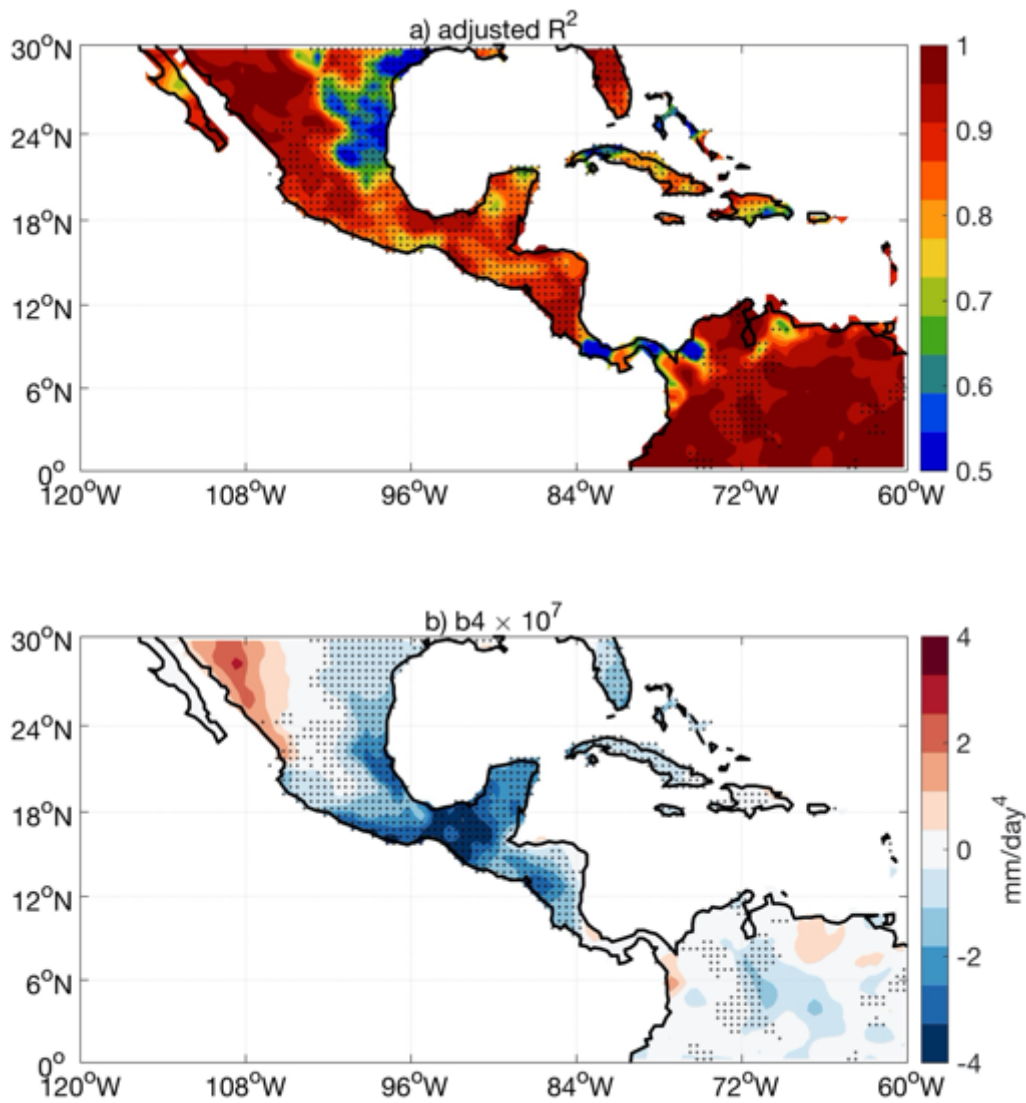


Figure 12

Performance of 4th order polynomial models on the climatological precipitation during rainy seasons. a) The adjusted R^2 resulted from fitted model in each grid. b) Coefficient in front of the 4th order term in each grid. Regions exhibiting MSD signals are shaded by black dots.

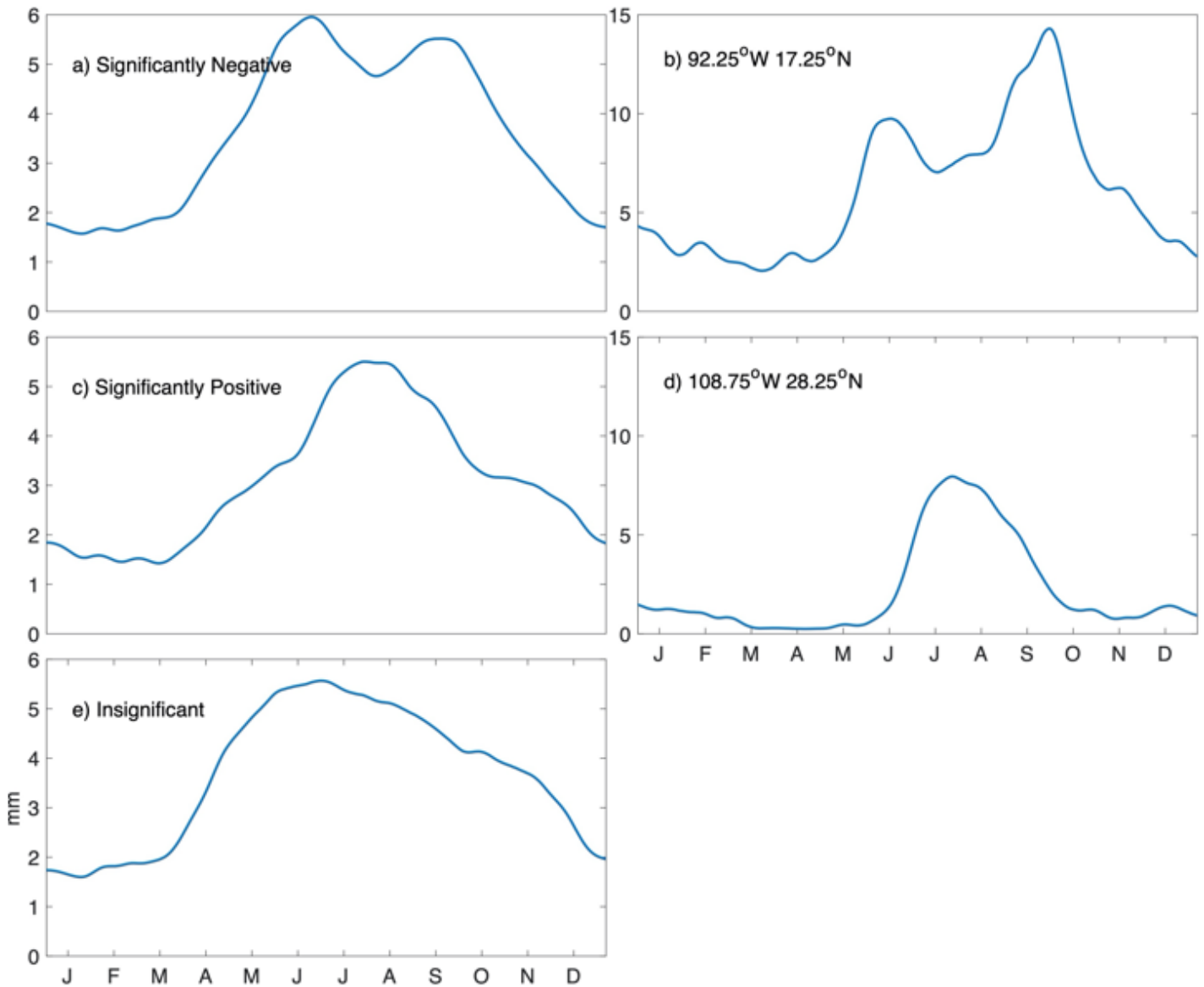


Figure 13

Spatially averaged annual climatology of precipitation with respect to different regions, including a) domain dominated by negatively significant b_4 according to Figure 11, b) the grid point dominated by the most negative b_4 , c) domain dominated by positively significant b_4 according, d) the grid point dominated by the most positive b_4 , and e) domain dominated by insignificant b_4 . A 31 – days moving average is applied to smooth each generated climatology.

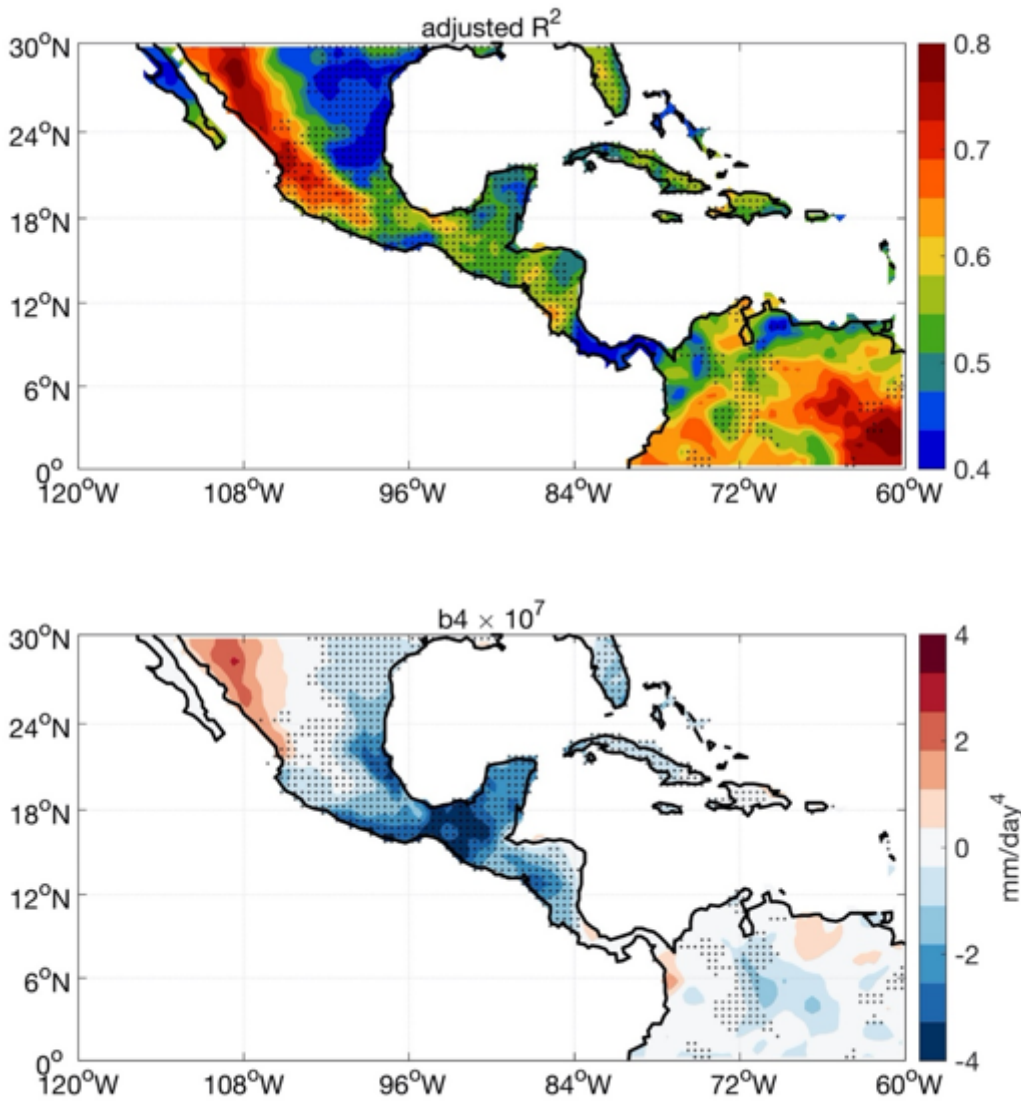


Figure 14

Performance of 4th order polynomial models on the annual precipitation during rainy seasons. a) Yearly averaged adjusted R^2 resulted from fitted models in each grid. b) Yearly averaged coefficients in front of the 4th order term in each grid. Regions exhibiting MSD signals are shaded by black dots.

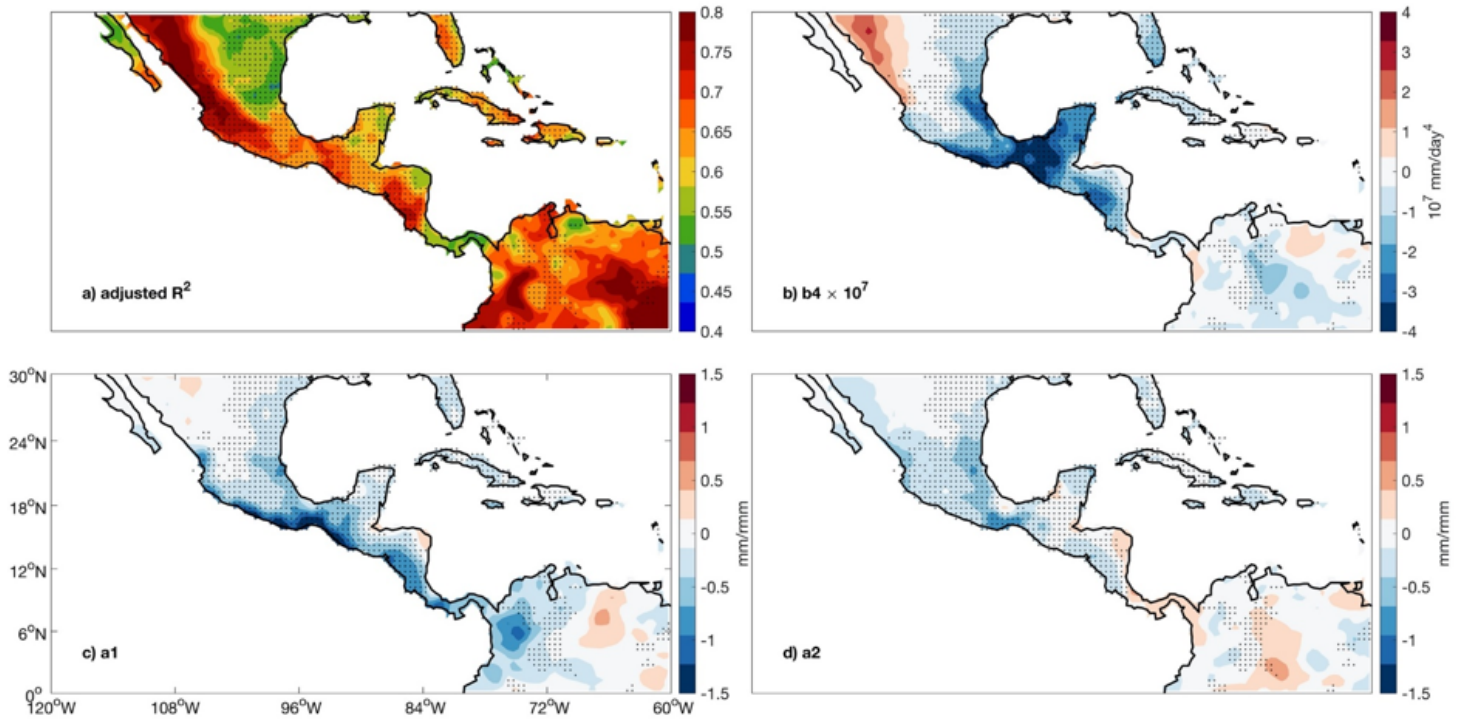


Figure 15

Performance of 4th order polynomial models with MJO covariates on the annual precipitation during rainy seasons. a) Yearly averaged adjusted R^2 resulted from fitted models in each grid. b) Yearly averaged coefficients in front of the 4th order term in each grid. Yearly averaged coefficients in front of c) RMM1 and d) RMM2 in each grid.

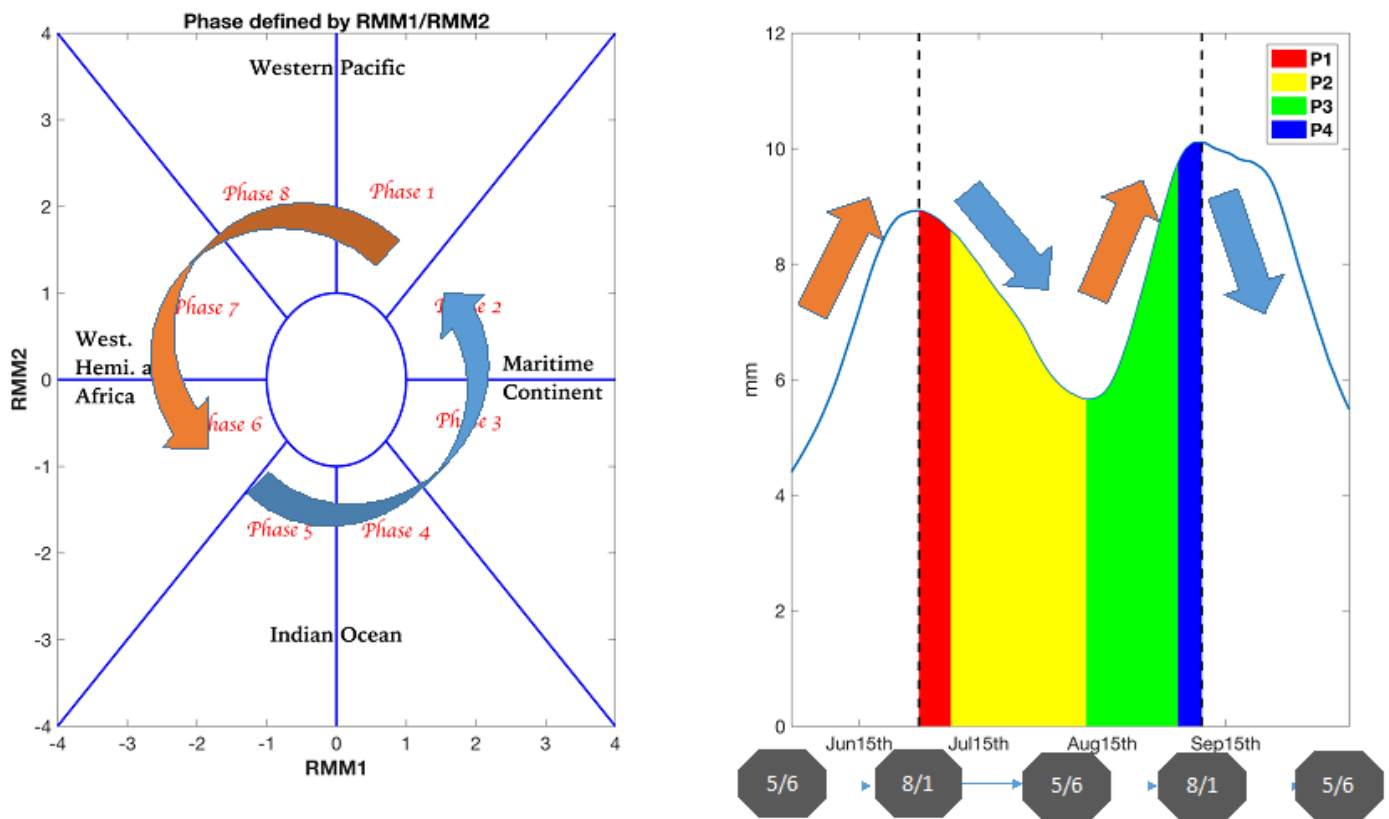


Figure 16

Synoptic illustration of the MJO's modulation on the MSD signals over Central America and Mexico. The increase (decrease) of precipitation during the change of MJO phases is indicated by orange (blue) arrow in left panel. The right panel is similar to Figure 8, with orange (blue) arrows indicating the increase (decrease) of precipitation and corresponding MJO phase changes labelled in the bottom.